

Application of Temperature-Sensitive Paint for transition detection on an NLF forward-swept wing under harmonic pitch oscillation at flight-relevant Mach and Reynolds numbers

Nils Paul. van Hinsberg^{1,*}, Ulrich Henne¹, Christian Klein¹

1: Dept. of Experimental Methods, Institute of Aerodynamics and Flow Technology, German Aerospace Center (DLR), Göttingen, Germany

*Corresponding author: nilsvanhinsberg@dlr.de

Keywords: laminar-turbulent transition, Temperature-Sensitive Paint, forward-swept wing, natural laminar flow, transonic flow, harmonic pitch oscillation, ETW.

ABSTRACT

To reduce the fuel consumption and emissions of next generation commercial aircraft, the highly promising natural laminar flow (NLF) technology is being implemented more and more frequently. By maintaining a laminar flow over the largest possible area of both wings through either passive or active measures, the overall aircraft friction drag over these surfaces can be significantly reduced, which results in a distinct increase in the aerodynamic performance of the aircraft. To raise the Technology Readiness Level of this laminar technology in aircraft design, an NLF forward-swept wing fuselage-belly-fairing configuration was designed in the KoPa 33 research initiative ECOWING. In the LuFo VI-2 successor project ULTIMATE, joint wind tunnel experiments in the European Transonic Windtunnel and Computational Fluid Dynamics simulations have been performed on this specific configuration. The various point-wise (e.g. unsteady pressure sensors, static pressure taps, temperature sensors, and accelerometers) and optical measurement techniques that were applied in the wind tunnel tests included also time-resolved cryogenic Temperature-Sensitive Paint (cryoTSP). This latter optical measurement technique was implemented to obtain in particular the location and dynamic motion of the boundary-layer transition on the upper (hence, suction) surface of the forward-swept wing model. The first test campaign, i.e. the performance test, demonstrated a clear influence of variations in flight relevant Mach and Reynolds numbers – both under on-design and off-design conditions – on the spanwise transition distribution, the resultant amount of laminarity over the wing, and the boundary layer transition mechanisms for a wide range of static pitch angles and during various quasi-steady pitch-sweeps at selected Mach and Reynolds numbers. In the current paper, the emphasis is placed on the TSP results of the subsequent dynamic test, in which the focus was shifted to the aerodynamic behavior of the NLF forward-swept wing while forced to perform a harmonic pitch oscillation using a newly-designed pitch oscillator. Besides isolated and combined variations in the Mach and Reynolds number, the influences of the mean angle, amplitude, and reduced frequency of the pitch oscillations were captured successfully by TSP. The analysis of the data using the “D0-method”, an alternative to the “DIT-method”, namely revealed distinct changes in both the location and dynamics of the transition line during pitching limit-cycle oscillations, induced by a separate altering of the value of each of the test parameters. Moreover, it was demonstrated that absolute motions of the transition location as small as $\mathcal{O}(10^{-4})$ m could accurately be resolved by the TSP technique.

1. Introduction

Besides an improvement of the thrust-specific fuel consumption (e.g. by the adoption of ultra-high bypass ratio of geared turbofan engines, by a (partial) electrification of the propulsion system, or using sustainable aviation fuels (Giesecke et al., 2018)) and the use of high-aspect-ratio wings to lower the induced drag (International Air Transport Association (IATA), 2023), the natural laminar flow (NLF) technology is a very promising third option to substantially reduce the emission pollution by next generation commercial transportation aircraft. By passively or actively maintaining a laminar flow over the largest possible area of both wings, the overall friction drag on these surfaces can be significantly reduced, which not only leads to a better aerodynamic performance of the aircraft, but also lowers its fuel consumption (Redeker et al., 1990; Fujino et al., 2003; Seitz et al., 2011; Crouch, 2015). Boundary layer suction, the application of special surface materials and coatings, wing tailoring, contour shaping of various wing sections, and the use of minuscule bumps close to the wing's leading edge are just a few of the many possible flow control mechanisms to achieve those goals, e.g. Saeed et al. (2010), Streit et al. (2015), and Krishnan et al. (2017). By giving each wing a forward sweep, the effective angle of their leading edges can be significantly reduced (Lange-Schmuckall, 2022). In doing so, the crossflow instabilities and attachment line contamination can be clearly weakened, which can be treated as being a very positive effect, as the presence of both phenomena would result in the occurrence of a transition to turbulence close to the leading edge (Joslin, 1998; Schlichting & Gersten, 2016). Hence, in the latter case the formation and maintenance of performance-relevant large regions with laminar flow over the wing surface would thus be hindered, making the application of the NLF technology in that case very challenging. The forward sweep thus allows for a realization of a combination of modern high cruise Mach and Reynolds numbers on the one side and NLF on the other.

To further raise the Technology Readiness Level (TRL) of this laminar technology in commercial transport aircraft design and thus be able to achieve the highest possible reduction in fuel consumption, the research initiative ECOWING (Wing Technology Validation for Ultra Green Aircraft, 2020-2021) and its successor project ULTIMATE (Ultra High Efficient Wing and Movables for Next Generation Aircraft, 2022-2026), implemented in the German Economic Stimulus Programme KoPa 33 and the sixth German Aeronautical Research Programme LuFo VI-2, respectively, pursue the detailed design of future laminar wings. To obtain a full understanding of the flight physics at on-design and off-design flight configurations in the complete flight envelope of a typical medium range aircraft, joined wind tunnel tests in the cryogenic European Transonic Wind Tunnel (ETW) in Cologne (Germany) and high-fidelity Computational Fluid Dynamics (CFD) simulations have been performed on a newly-designed high-performance forward-swept wing fuselage-belly-fairing configuration, hereupon abbreviated as NLF-FSW. The wing is given a large aspect ratio to improve the aerodynamic performance and to increase the cruise Mach number in

comparison to configurations with conventional NLF-wing designs. In this way, the reduction of the life cycle CO₂ emissions can be improved even more than by using solely the NLF technology. The measurement data is first of all intended to confirm the correct wing design at realistic flight conditions. In addition, it is used to validate high-fidelity Computational Fluid Dynamics (CFD) tools for robust and accurate prediction of the complex and transient laminar-turbulent transition behaviour over NLF-wings.

For the experimental assessment (i.e. visualisation, detection, and analysis) of the time-resolved behaviour of the chordwise position of laminar-turbulent transition in the surface boundary layer along the wing's span for varying flight conditions (i.e. Mach number, Reynolds number, pitch angle, etc.), large areas of the upper surface of NLF forward-swept wing model were covered with cryogenic Temperature-Sensitive Paint (cryoTSP) (Klein et al., 2017). TSP is an optical temperature measurement technique based on the thermal quenching process of excited dye molecules embedded in a binder material, and is widely used in conventional wind tunnel tests (e.g. Liu, Sullivan, et al. (2021)). The great advantage of this optical measurement technique is the ability to obtain global temperature distributions on the surface of a wind tunnel model with a high spatial resolution. In case high-speed cameras are used, the recorded data have a high temporal resolution as well, which makes TSP highly favoured over punctual measurements by for example thermocouples. Since the naturally established difference between the recovery temperature of laminar and turbulent boundary layers on the model surface is typically too small to be able to detect the boundary layer transition with TSP, it is necessary to introduce an artificial increase of the adiabatic wall temperature difference by producing a temperature difference between the model surface - coated with TSP - and the incident flow. The main focus of the first measurement campaign (hence, the "performance test") in the project ULTIMATE, conducted in 2022 in ETW and described in detail in Van Hinsberg et al. (2024), was on the analysis of the influence of a variation in Reynolds and Mach numbers - both under on-design and off-design conditions - over a wide range of static pitch angles on the spanwise distribution of the boundary-layer transition pattern. In addition, three different methods to achieve the necessary and sufficiently large temperature difference between the TSP-coated model surface and the flow were furthermore tested for comparison of their applicability and efficiency for TSP under cryogenic test conditions.

The current paper addresses the results of the second TSP test campaign in ETW on the NLF forward-swept-wing combined with a fuselage-belly-fairing. In contrast to the "performance test", a pitch oscillator, specially designed within this project for dynamic model testing in ETW, was used to set the wind tunnel model into a forced harmonic pitch oscillation. The first part of this paper puts the focus on the principle of TSP, the measurement equipment, and the wind tunnel model. The data acquisition and data (post-)processing methods are briefly discussed as well. In the second part, the obtained TSP results are presented and analysed. This includes in particular

the influence of the amplitude and (reduced) frequency of the forced harmonic pitch oscillation of the model, as well as the variation in the mean pitch angle around which those pitch oscillations were performed. All but one of those unique measurements were carried out at combinations of two free-stream Mach and Reynolds numbers, i.e. $M = 0.73$ and 0.78 and $Re_c = 10 \times 10^6$ and 16×10^6 , whereby the latter are based on the mean chord length of the wing. The isolated effects of a variation of each of these two dimensionless flow parameters are also shown and discussed.

2. Experimental methods

2.1. European Transonic Windtunnel and forward-swept wing fuselage-belly-fairing model

The measurements were conducted in the ETW, a circulating (Göttingen-type) transonic wind tunnel test facility that is operated with cold nitrogen as test gas. Its test section has a rectangular cross-section of $2.0 \times 2.4 \text{ m}^2$ and measures 9 m in length. Model-scale Mach and Reynolds numbers of $M = 0.15\text{--}1.35$ and $Re_{b=1.3m} \leq 85 \times 10^6$ (with b the reference length of the wind tunnel model), respectively, can be achieved through pressurisation of the test gas up to $p_0 = 450 \text{ kPa}$ in combination with a decrease of the gas temperature down to values as low as 110 K .

The wind tunnel model is an NLF forward-swept wing combined with a fuselage-belly-fairing, as shown in Fig. 1. The main dimensions of the tapered wing are listed in Tab. 1. The complete model,



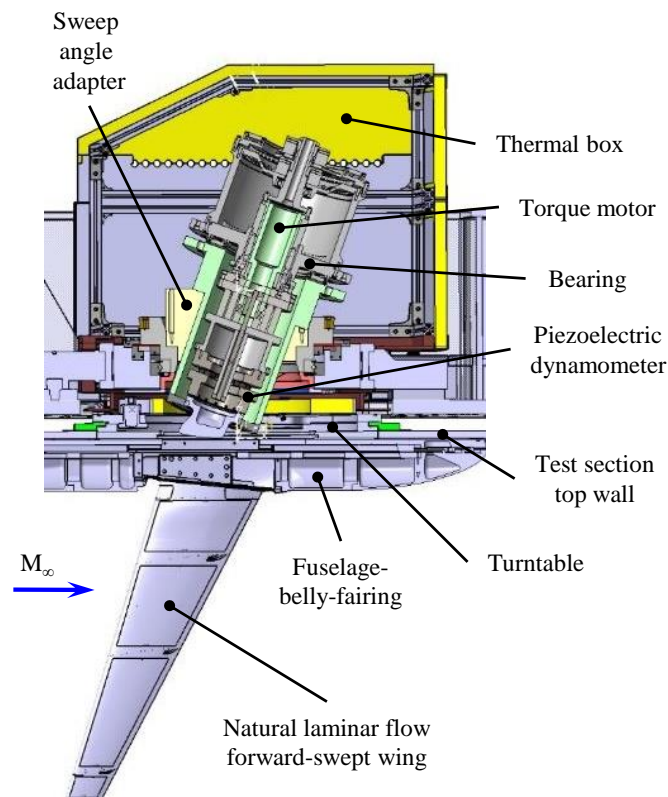
Figure 1. Setup of the forward-swept wing model in ETW. The orange fields on the upper wing are the four pockets with cryoTSP for the determination of the spatial distribution of the laminar-turbulent transition location.

together with the peniche – mounted between the model and the test section – were fabricated of steel suitable for a cryogenic environment. The wing was connected to a pitch oscillator (Fig. 2) with which the former can be set into a forced harmonic pitch oscillation with a specific amplitude and frequency around an arbitrary pre-set mean pitch angle. This allows the measurement of not

Table 1. Main dimensions of the NLF forward-swept wing.

Quantity	Value
Root chord length (c_{root}) / m	0.374
Tip chord length (c_{tip}) / m	0.127
Mean chord length (\bar{c}) / m	0.28653
Wing half span (b) incl. tip / m	1.257
Aspect ratio (AR)	9.475
Leading edge sweep angle (φ_{LE}) / °	-17.0
Trailing edge sweep angle (φ_{TE}) / °	-27.0

only the highly dynamic motion-induced aerodynamic loading on the wing, but at the same time also of the time-resolved dynamic behaviour of the laminar-turbulent transition of the boundary layer on its surface. The pitch oscillator together with the wing, the fuselage-belly-fairing, and the peniche were mounted on a turntable that was integrated in the top wall of the test section. By changing the angle of the turntable the mean angle of incidence of the complete wind tunnel model could be varied.

**Figure 2.** Overview of the pitch oscillator setup.

The cryoTSP sensor was applied to four separate areas (i.e. the orange fields in Fig. 1) on the suction side of the wing. After delivery of the model, the inner surfaces of the four recessed pockets with a mean depth of $120\ \mu\text{m}$ underwent first of all a plasma activation treatment. In a second step, they were subsequently filled by a primer thermal layer (mean thickness of $20\ \mu\text{m}$), an additional white layer of $40\ \mu\text{m}$ thickness for the electrical insulation against the model structure, a thin, i.e. $10\ \mu\text{m}$ thick layer consisting of a mixture of Carbon Nanotubes (CNT) and a polyurethane solution, a screen layer that assures both a thermal insulation and the enhancement of the TSP signal owing to its high reflectivity, and finally the actual TSP active-layer. In combination with thin copper tapes and electric wires in the model and one or multiple external power supplies, the CNT layer with its low electric resistance was used as an additional heating method during the "performance test" of the forward-swept wing (Van Hinsberg et al., 2024). Its purpose was to generate a homogeneous and constant temperature increase over the model surface from the inside of the model (Iijima, 1991; Klein et al., 2014). One of the outcomes of the "performance test" was the proof that CNT-heating is generally too slow to accurately resolve the fast changes of the laminar-turbulent transition location in chordwise direction along the span of the model with high-speed cameras during high-frequency forced harmonic pitch oscillations. For the current "dynamic test", the copper tapes and electric wires were thereupon removed, thereby inactivating the CNT-heating. Because of its black colour, the current main purpose of the CNT layer was the enhancement of the indirect internal heating of the TSP layer by light absorption from two external infrared laser (Van Hinsberg et al., 2024). In between the screen layer and the TSP active-layer, multiple markers were positioned at predefined locations, their purpose being twofold. On the one hand, they are required to allow an accurate alignment of the TSP images from the two cameras, from which a precise mapping onto the three-dimensional model grid can be achieved. On the other hand, the markers enable an exact temporal optical tracking of the model position and possible model deformation through the Image Pattern Correlation technique (IPCT). In a final step, the top layer was polished to minimise surface imperfections and to obtain a step-free surface finish of the TSP coating at the desired mean overall thickness of $120\ \mu\text{m}$. This resulted in a mean deviation of the coated model contour to the target one of less than $8\ \mu\text{m}$.

Apart from cryoTSP, the forward-swept wing was also equipped with various point-wise measurement techniques such as chordwise-staggered unsteady pressure sensors (Kulite[®]) on the wing suction side at three spanwise sections, static pressure taps in a staggered configuration along one complete cross-section of the wing adjacent to the innermost TSP field, temperature sensors in both the TSP coating and the interior of the wing, as well as multiple accelerometers at various locations in the wing. An external 5-component half-model balance was furthermore used to obtain the global normal and axial forces, as well as the overall moments in pitch, roll, and yaw that acted on the model. In addition, the pressure side of the wing was covered by multiple markers in ten spanwise sections to measure the model deformation using the in-house (ETW) Stereo Pattern

Tracking (SPT) technique (Semmelmann et al., 2013).

2.2. Cryogenic Temperature-Sensitive Paint

The working principle of a TSP sensor is based on the thermal quenching process of dye molecules that are embedded in a binder material (Liu, Sullivan, et al., 2021). Through the absorption of light by these molecules at the appropriate wavelength, they are transferred to a higher excited energy level. Two possible internal relaxation processes may occur. Either the excited dye molecules return to their ground state while emitting light at a longer wavelength than required for their excitation, i.e. luminescence. Or the internal relaxation takes place radiationless, in which case we speak of thermal quenching. Since the latter relaxation pathway is temperature-dependent, the luminescent intensity of the emitted light from the TSP dye I reduces with increased temperature and is thus a measure for the surface temperature T . This behaviour can be approximated by the Arrhenius relation:

$$\ln\left(\frac{I}{I_{ref}}\right) = \frac{E_{nr}}{R} \left(\frac{1}{T} - \frac{1}{T_{ref}}\right) \quad (1)$$

where $I_{ref} = I(T_{ref})$ is the luminescent intensity at a certain reference temperature T_{ref} , E_{nr} is the activation energy for the non-radiative process, and R is the universal gas constant. In general, one can thus say that the higher the temperature of the model surface and thus also of the TSP paint, the stronger is the thermal quenching process that takes place in the dye and the lower its emission intensity will be.

A temperature-sensitive paint based on a Ruthenium complex embedded in a polyurethane binder was used for the current TSP measurements in ETW. This so-called cryoTSP was excited with blue light in a wavelength range of $\lambda = 420\text{-}520$ nm, upon which it emitted red light in the range of $\lambda = 590\text{-}700$ nm (Egami et al., 2012). As mentioned in section 1, a sufficiently large temperature difference between the TSP active layer on the model surface and the incoming flow is required to be able to distinguish between the laminar and turbulent regions of the boundary layer over the upper wing surface in the TSP recordings. The direct comparison of the TSP results of the "performance test", obtained by the three tested principles to produce the necessary artificial temperature difference between the TSP-layer on the model's surface and the flow (i.e. *temperature step*, *CNT-heating* (Klein et al., 2014; Goodman et al., 2016; Liu, Salazar, & Crafton, 2021), and *IR-laser heating*), has shown that the transition pattern for static pitch angles of the wind tunnel model can be captured successfully by each one of them with close agreement among all three (Van Hinsberg et al., 2024). However, in the same wind tunnel test campaign it also became clear that the principle of heating by CNT is generally too slow to be able to accurately resolve the fast changes of the laminar-turbulent transition location in the time-resolved TSP images during high-frequency forced harmonic pitch oscillations. This method was therefore omitted in the currently described

"dynamic test" and only the two remaining heating principles were applied: temperature step (*T-step*) and heating by infrared lasers (*IR-laser heating*). The first principle, i.e. the *T-step*, is realised in ETW by a temporal variation of the injection rate of liquid nitrogen, as it leads to an increase or decrease of the nitrogen test gas temperature. Despite the good contrast in image intensity between the laminar and turbulent regions and thus the highly accurate results of the transition location that are yielded by this method, its main disadvantage is the additional run time of the wind tunnel to change the temperature of the inflow. Unfortunately, it is also this long reaction time that makes the method unsuited for tracking the transition location in time on a harmonically oscillating wind tunnel model at high frequency, owing to which this method was only used for TSP measurements at static pitch angles. Moreover, this increase or decrease of the flow temperature by 1-2% induces a small change in the Reynolds number of approximately 2-3%. *IR-heating*, on the other hand, is a relatively new method based on an external (and indirect internal) heating of the TSP sensor with the use of one or more powerful infrared lasers (Thiessen & Schülein, 2019). In comparison to the *T-step*, this method has the large advantage of being non-intrusive and its fast reaction time makes it furthermore well suited for time-resolved TSP tests on harmonically oscillating wind tunnel models.

2.3. Test equipment

A water-cooled blue diode laser (LDM*blue* by Laserline GmbH, $P_{max,blue} = 250$ W, emission peak at $\lambda = 445 \pm 20$ nm) was used as the main TSP excitation light source in all tests at $Re_{\bar{c}} = 10 \times 10^6$, while the TSP dye molecules were excited by blue LEDs (Luxeon V Star, emission peak at $\lambda = 480$ nm) at $Re_{\bar{c}} = 16 \times 10^6$. This switch from one illumination source to the other between both Reynolds numbers was required, since the decrease in flow temperature from $T = 170$ K ($Re_{\bar{c}} = 10 \times 10^6$) to 124 K ($Re_{\bar{c}} = 16 \times 10^6$) would have asked for a significant power increase of the blue diode lasers that could have resulted in a fast degradation of the TSP sensor. Both the blue laser and the LEDs were operated in a constant current mode. To remove the light in the longer wavelength range that was emitted by the LEDs, each one of them was equipped with a low-pass filter (LOT-Oriel D475/50X, maximum transmission ca. 80%). The TSP luminescence was acquired using two 12-bit 1 megapixel Photron FASTCAM Mini AX200 high-speed cameras. Both used a Canon objective (EF 35 mm 1.4 L USM), a 590FG05-25 (LOT-Oriel) optical high-pass filter, and an 875SP-50 (Edmund Optics) IR-blocker, the latter two having a maximum transmission of about 90%. The LEDs and the cameras were placed at a distance of about 1-1.2 m from the upper surface of the model. Synchronisation between the TSP equipment and the ETW was controlled by a RS232 connection.

For the method of *IR-laser heating*, two external water-cooled IR-lasers (LDF 6000-60, each with a maximum power of $P_{max,IR} = 5$ kW) were used. Specially-designed coupling optics by Laserline GmbH brought the laser light of both the blue diode laser and the two IR-lasers into the

cryogenic wind tunnel, after which the laser beams were routed by heated fibres inside the cryogenic atmosphere of the test section towards optics that were positioned at test section side wall windows (Hensch et al., 2023). The optics had fixed focal lengths and produced rectangular beams of about $1000 \times 400 \text{ mm}^2$ in the model plane that was used to heat the TSP surface or excite the TSP dye molecules. The power of each IR-laser was set to its maximum value, while the blue laser generated a reduced power of $P_{blue} = 50 \text{ W}$ to avoid a saturation of the CMOS image sensor of the cameras.

2.4. Experimental conditions and data acquisition

The "dynamic test" focused on two flight relevant Reynolds numbers, i.e. $Re_{\bar{c}} = 10 \times 10^6$ and 16×10^6 , while three Mach numbers were selected, hence, $M = 0.70, 0.73,$ and 0.78 . As listed in Tab. 2, four kinds of measurements have been performed. To gather as much aerodynamic data as possible

Table 2. Wind tunnel test conditions for "dynamic test" in ETW.

Test series	$Re_{\bar{c}} (\times 10^6)$	M	$\bar{\alpha} / ^\circ$	$\Delta\alpha_{pp} / ^\circ$	k
Static pitch angle	10	0.73, 0.78	-0.06, 0.93 (± 0.02)	-	-
	16	0.70	-0.05	-	-
	16	0.73	-3.48, -0.05, 0.92	-	-
	16	0.78	-3.50, 0.92 (± 0.01)	-	-
Quasi-steady pitch angle sweep	10, 16	0.70, 0.73, 0.78	$-4.01^a \rightarrow 4.02^a (\pm 0.01)$	-	-
Quasi-steady Mach number sweep	10	$0.735^a \rightarrow 0.774^a \rightarrow 0.704^a$	0.81^a	-	-
Harmonic pitch oscillation	10	0.73, 0.78	-0.06, 0.93 (± 0.02)	0.2, 0.4, 0.6, 0.8, 1.0	0.3
	10	0.73, 0.78	-0.06, 0.93 (± 0.02)	0.2	0.1, 0.3, 0.4, 0.6
	10	0.73, 0.78	-0.06, 0.93 (± 0.02)	0.1	0.8
	16	0.70	-0.05	0.2, 0.4, 0.6, 0.8, 1.0	0.4
	16	0.73	-3.48, -0.05, 0.92	0.2, 0.4, 0.6, 0.8, 1.0	0.3
	16	0.73	-3.48, -0.05, 0.92	0.2	0.1, 0.2, 0.3, 0.4
	16	0.73	-3.48, -0.05, 0.92	0.1	0.8
	16	0.78	-3.50, 0.92 (± 0.01)	0.2, 0.4, 0.6, 0.8, 1.0	0.3
	16	0.78	-3.50, 0.92 (± 0.01)	0.2	0.1, 0.2, 0.3, 0.4
	16	0.78	-3.50, 0.92 (± 0.01)	0.1	0.8

^a Uncorrected for any blockage effect.

during the wind tunnel run time, both quasi-steady pitch angle sweeps and Mach number sweeps were conducted. During pitch angle sweeps, the wind tunnel model is moved continuously with a predetermined constant angular pitch velocity in the so-called pitch-traverse mode. For all combinations of Mach and Reynolds number, the pitch sweep direction was from negative to positive pitch angles with a constant angular velocity of $\Delta\alpha_{sweep} = +0.12^\circ/\text{s}$ within the range of pitch angles of $-4.01^\circ \leq \alpha \leq 4.02^\circ$. The influence of the Mach number was studied by one single Mach sweep at $Re_{\bar{c}} = 10 \times 10^6$ and $\alpha = 0.81^\circ$, and consisted of two parts: an increase from $M = 0.735$ to 0.774 that was directly followed by a decrease down to $M = 0.704$, both at an equal constant rate. However, the majority of the "dynamic test" campaign focused on the wind tunnel model perform-

ing a forced harmonic pitch oscillation around a constant pre-set mean pitch angle, see Tab. 2. For each selected combination of Mach and Reynolds number, both the reduced pitch frequency $k = (\pi f_{pitch} \bar{c}) / U_\infty$ (where f_{pitch} equals the model's dimensional pitch frequency and U_∞ the free-stream velocity) and the peak-to-peak amplitude $\Delta\alpha_{pp}$ were selected as independent variables. Hence, either the former was changed between $0.2^\circ \leq \Delta\alpha_{pp} \leq 1.0^\circ$ in steps of $\Delta\alpha_{pp} = 0.2^\circ$ while the latter was kept constant at $k = 0.3$ or 0.4 , or the latter was varied in the range of $k = 0.1$ – 0.8 with a step size of $\Delta k = 0.1$ and 0.2 at a constant peak-to-peak amplitude of $\Delta\alpha_{pp} = 0.1^\circ$ or 0.2° . Each block that includes the variation of either the peak-to-peak amplitude or the reduced pitch frequency was preceded by a single measurement at the static mean pitch angle, hence, without a superimposed forced harmonic pitch excitation.

Both cameras were operated with a frame rate of either $f_{cam} = 50$ Hz (quasi-steady pitch angle and Mach sweeps) or 2 kHz (static pitch angles and harmonic pitch oscillations). The exposure time of the recorded images was $t_{exp} = 200 \mu s$, independent of the frame rate of the cameras. Each sweep and each pitch oscillation was performed twice at exactly the same flow conditions: once without heating by the temperature step or by the IR-lasers for the recording of the *reference* images, and once with heating for the acquisition of the *run* images. The heating was therefore switched on between the last reference and the first run image. During all sweep tests, an equal amount of 3640 *reference* / *run* images were acquired per test point, while 4368 *reference* and *run* images were recorded at each static mean pitch angle and during each harmonic pitch oscillation.

3. Data post-processing

Depending on whether the static pitch angles, quasi-steady sweeps, or the harmonic pitch oscillations were evaluated, different post-processing methods were used to automatically detect the boundary-layer transition location in the TSP recordings.

The first method, applied to the TSP images that were recorded at static pitch angles or during the quasi-steady pitch angle and Mach number sweeps, has been described in detail in Van Hinsberg et al. (2024). It mainly follows the transition detection algorithm described by Costantini et al. (2021), with the additional implementation of some minor modifications for an optimised application to the current TSP data. The algorithm is predominantly based on the capability of detecting the maximum value of the gradient of the normalised luminescent intensity ratio in the transition region along the chord of the wing in a very accurate and robust manner. It should be mentioned at this point, that for the static pitch angles, all *reference* and *run* images within one test run (hence, one polar) were used to determine one single mean two-dimensional *reference* and *run* image per camera. Regarding the Mach number and pitch angle sweeps, time-averaged *reference* and *run*

images were calculated per block of 10 sequential recordings. This resulted in five time-averaged *reference* and *run* images per camera and second of recording time.

Since the focus of the current paper is mainly on the dynamic, i.e. time-resolved behaviour of the chordwise transition location along the span of the NLF-FSW while it performs a harmonic pitch oscillation, the various post-processing steps that have been carried out one after the other in order to be able to visualise and analyse this time-dependent transition behaviour are described in more detail. These include:

1. the analysis of the specific part of the time series of the pitch angle during which the TSP *reference* and *run* images were recorded by both cameras. This includes the exact pinpointing of all zero-crossings, the calculation of the precise mean harmonic pitch frequency, and the assignment of a phase and pitch amplitude to each TSP image by using a "mean" sinusoidal pitching function.
2. the mapping of each TSP image onto a single pitching period based on the assigned phase in the previous analysis step.
3. the division of that period into 144 equally spaced bins, each with a uniform width of $\Delta\varphi = 2.5^\circ$. This means that the mean phase of the first bin is located at $\bar{\varphi} = 1.25^\circ$, while that one of the last bin (i.e. bin no. 144) is found at $\bar{\varphi} = 358.75^\circ$.
4. the calculation of the phase-averaged two-dimensional *reference* and *run* images of both cameras per bin.
5. the alignment of the phase-averaged images of both cameras to the known TSP marker positions on the model surface, their merging into a single phase-averaged image, and the mapping of each resultant two-dimensional image onto a three-dimensional grid of the upper surface of the forward-swept wing. All three steps were accomplished for all phase-averaged *reference* and *run* images by using the DLR in-house software package *ToPas* (Costantini et al., 2021). Despite the tapered shape of the wing model, a constant resolution of $\Delta(x/c) \sim 0.5\%$ could be achieved in the chordwise direction at each spanwise grid location.
6. the building of the phase-averaged intensity ratio image per bin by division of each mapped two-dimensional *run* image by its corresponding *reference* image. This enhances the differences between the laminar and turbulent regions and compensates for any inhomogeneities of the excitation light or of the thickness of the overall TSP-layer.
7. the calculation of the ratio-by-ratio phase-averaged intensity image using the "*DO method*", an alternative to the "*Differential Infrared Thermography (DIT) method*". Because of its ability to reveal rapidly changing temperature gradients over time that are induced by transition in the surface boundary layer, the "*DIT method*" is mostly applied to globally detect the laminar-turbulent transition motion on the surface of a (dynamically) moving wind tunnel model

(e.g. Weiss et al. (2020); Yorita et al. (2020); Wolf (2023)). In brief, the "*DIT method*" is based on the subtraction or division of two subsequently recorded luminescent intensity run (or intensity ratio) images that correspond to slightly different angles of pitch of the wind tunnel model. The resulting change of the surface temperature can be mostly attributed to the movement of the boundary-layer transition. However, since the pitch amplitude of the wind tunnel model was that small in the current "*dynamic test*", the application of the "*DIT method*" to subsequent phased-averaged intensity ratio images did not lead to clear enough changes in the surface temperature to determine the movement of the boundary-layer transition in a precise manner. A distinct improvement was obtained by using the "*D0 method*", in which case each of the 144 phase-averaged intensity ratio images is divided by the same "*reference*" phase-averaged intensity ratio image, in this case the one that belongs to the first bin. For three selected mean phases within one pitch oscillation period the results of the "*D0 method*" are shown in Fig. 3, whereby image (a) is taken as the "*reference*" phase-averaged intensity ratio image. The appearance of brighter areas at the transition location in the "*D0-images*",

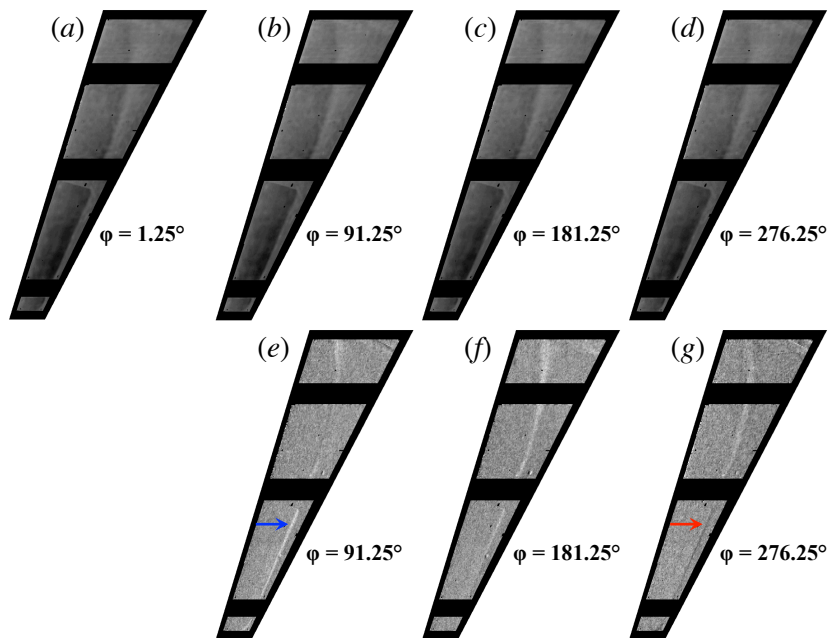


Figure 3. Comparison between phase-averaged intensity ratio images (upper row) and ratio-by-ratio phase-averaged intensity images or "*D0 method*" (lower row) for selected mean phases within one pitch oscillation period. Image (a) is taken here as the "*reference*" phase-averaged intensity ratio image for the "*D0 method*". Test conditions: $Re_{\bar{c}} = 10 \times 10^6$, $M = 0.78$, $\bar{\alpha} = 0^\circ$, $\Delta\alpha_{pp} = 1.0^\circ$, and $k = 0.30$.

exemplary marked by the blue arrow in Fig. 3e, denotes a movement of the transition location in upstream direction with respect to the transition location of the first phase-averaged bin, while darker areas (e.g. marked by the red arrow in Fig. 3g) signal a downstream motion. As becomes obvious, the "*D0 method*" does not work to calculate the spanwise distribution of the transition location for the first bin. In this case, those values were determined by the

same method as used for the analysis of TSP recordings obtained at static pitch angles and during the quasi-steady pitch angle and Mach number sweeps.

8. the normalisation of the three-dimensional ratio-by-ratio phase-averaged intensities to values between 0 and 1. For the uncoated regions in between neighbouring TSP fields, for which no signal of the TSP sensor was available, a linear interpolation of the normalised intensity ratio in spanwise direction from its neighbouring non-zero values was applied. In contrast, a constant normalised intensity ratio was set in the outer wing regions, i.e. close to the leading/trailing edge and wing root/tip. The value of this constant normalised intensity ratio was chosen to be equal to the value at the nearest chordwise and spanwise location, respectively, at which a TSP sensor was available.
9. the application of two mean spatial filters with sizes of $(x \times y) = (4 \times 1)$ and (9×1) and a discrete two-dimensional Laplace operator in chordwise direction at each spanwise location to improve the signal-to-noise ratio of the normalised ratio-by-ratio phase-averaged intensity distribution.
10. the calculation of the derivative of the filtered normalised ratio-by-ratio phase-averaged intensity distribution in chordwise direction along the span of the wing.
11. the evaluation of the actual transition position $x_{Tr}(y)/c$ at the mean time instant between subsequent bins by locating the maximum slope of the normalised ratio-by-ratio phase-averaged intensity distribution. We thereby make use of multiple plausibility criteria to ensure a correct detection and selection of the global maximum of the normalised ratio-by-ratio phase-averaged intensity distribution, in particular in those regions at which turbulent wedges were present (Costantini et al., 2021).

4. Results and discussion

In the following, the effect of variations in the values of the various model (hence, amplitude, mean angle, and reduced frequency of the harmonic forced pitch oscillation of the model) and flow (i.e. Mach and Reynolds number) parameters on the dynamics of the spanwise distribution of the transition location is presented and discussed.

4.1. Variation in pitch oscillation amplitude

Fig. 4 presents the processed results of the surface distribution of the recorded luminescent intensity of the cryoTSP sensor for sixteen mean phases of the pitch oscillation period, exemplary for $\Delta\alpha_{pp} = 1.0$. The Reynolds and Mach number of the incoming free-stream were kept constant at $Re_{\bar{c}} = 10 \times 10^6$ and $M = 0.78$, respectively, while the mean angle around which the model was

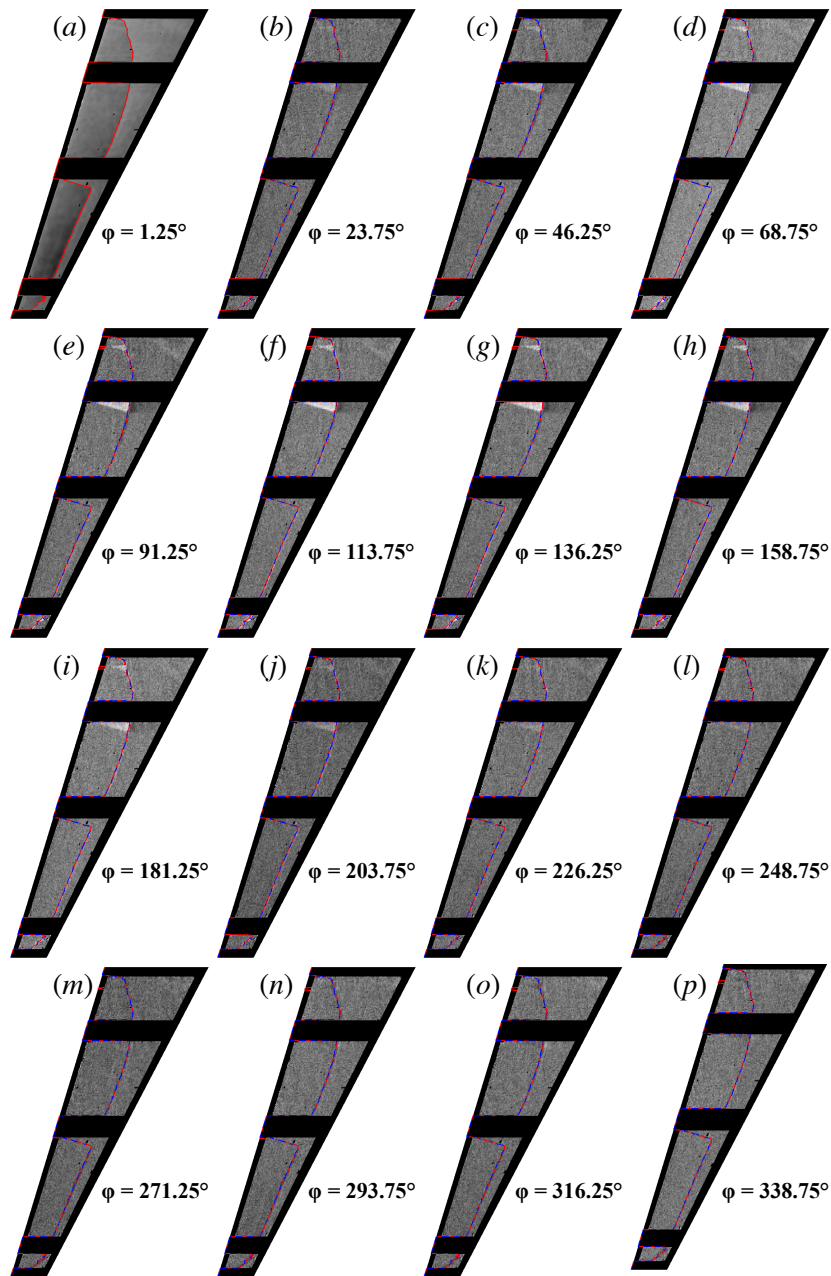


Figure 4. Motion of the laminar-turbulent transition pattern in the boundary layer over the upper surface of the NLF-FSW wing over one pitch oscillation period (flow from left to right). Test conditions: $Re_{\bar{c}} = 10 \times 10^6$, $M = 0.78$, $\bar{\alpha} = 1^\circ$, $\Delta\alpha_{pp} = 1.0^\circ$, and $k = 0.30$. The dashed blue line in the images (b) to (p) corresponds to the transition pattern at $\bar{\varphi} = 1.25^\circ$ (i.e. image (a)), while the solid red line represents the laminar-turbulent transition pattern at the specific selected mean phases.

pitched at a reduced frequency of $k = 0.3$ was set to $\bar{\alpha} = 1^\circ$. The first image, i.e. at $\bar{\varphi} = 1.25^\circ$, shows the combination of the phase-averaged surface intensity ratio and the detected laminar-turbulent transition location along the span of the wing (red solid line). This images was taken as "reference" phase-averaged intensity ratio image for the application of the "D0 method" on the recorded images

at all other mean phases. In the remaining images (b) to (p), the solid red line corresponds to the laminar-turbulent transition pattern at the specific selected mean phase that was calculated based on the shown normalised three-dimensional ratio-by-ratio phase-averaged intensities. To allow for a qualitative analysis of the dynamics of the transition location along the wing span over one pitch oscillation period, the transition pattern at $\bar{\varphi} = 1.25^\circ$ (i.e. image (a)) has been added to those images as well as a dashed blue line. By visual comparison of both transition lines, it becomes clear that for this specific combination of mean pitch angle, pitch oscillation amplitude, and reduced pitch frequency the strongest variations in the spanwise transition location occur close to the tip of the wing.

Figure 5 shows the quantitative spanwise distribution of the detected laminar-turbulent transition location in the surface boundary layer for all five investigated pitch oscillation amplitudes between $\Delta\alpha_{pp} = 0.2^\circ$ and $\Delta\alpha_{pp} = 1.0^\circ$. In each of the five images, the spanwise transition lines of all 144 equally spaced mean phases within one time-averaged pitch oscillation period (hence, from $\bar{\varphi}_1 = 1.25^\circ$ to $\bar{\varphi}_{144} = 358.75^\circ$) are presented using different colours. The comparison of the development of the spanwise transition curves for each of the five pitch oscillation amplitudes clearly shows that $\Delta\alpha_{pp}$ has its strongest influence on the dynamics of the transition location over the most outbound TSP field, i.e. near the tip of the wing. In this region, a distinct up- and downstream shift of the boundary between the laminar and turbulent region is seen to take place over one period of the pitch oscillation. In addition it is noted that this motion of the transition location increases with increased oscillation amplitude. In contrast, the curves in Fig. 5 also indicate that over the remaining, more inbound parts of the wing only a minor repositioning of the global transition location takes place for each tested pitch oscillation amplitude. The narrow dip in the curves for $0.176 \leq y/d \leq 0.189$ for the three lowest pitch oscillation amplitudes results from the presence of a turbulent wedge on the inbound TSP field at that location, causing the transition to locally move upstream.

The results from Fig. 5 were subsequently used to calculate the non-dimensional fluctuation of the laminar-turbulent transition location $\Delta x_{Tr}/c$ along the wing span for each mean phase $\bar{\varphi}$, defined as

$$\frac{\Delta x_{Tr}}{c} \Big|_{y/b} (\bar{\varphi}) = \frac{x_{Tr}}{c} \Big|_{y/b} (\bar{\varphi}) - \overline{\frac{x_{Tr}}{c}} \Big|_{y/b} \quad (2)$$

where $\overline{(x_{Tr}/c)}|_{y/b}$ equals the mean transition location over the complete pitch oscillation period at the spanwise location y/b . The outcomes are presented in Fig. 6 for all tested oscillation amplitudes at five spanwise locations between $y/b = 0.240$ (i.e. close to the root of the wing) and $y/b = 0.955$ (hence, near the wing tip). To assure a clear and concise display of the data, only the results of every third mean phase bin are shown. From this figure, several interesting aspects with respect to the quantitative fluctuations of the transition location along the selected spanwise locations can

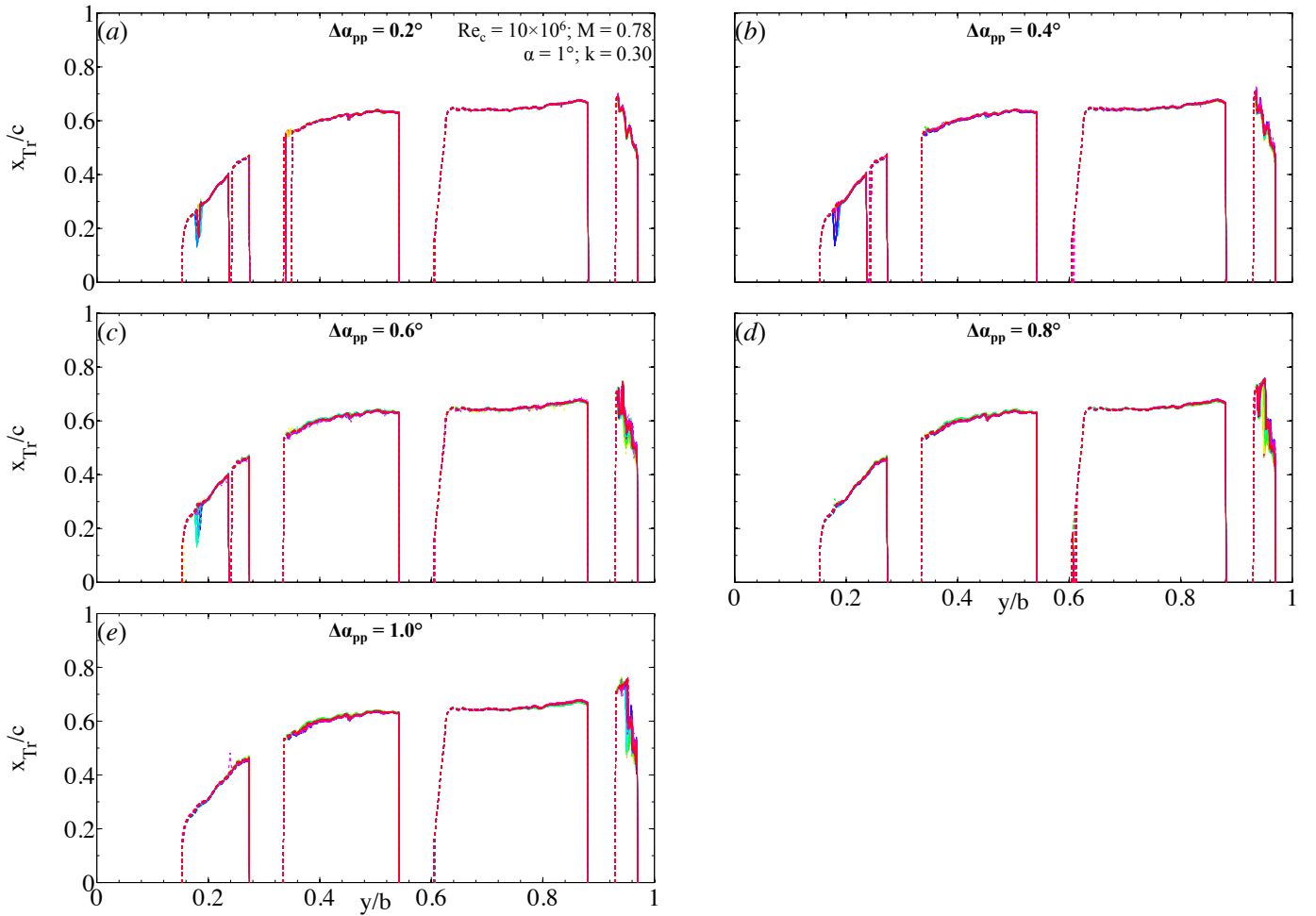


Figure 5. Overlay of spanwise distribution of the non-dimensional transition location x_{Tr}/c in the boundary layer over the upper surface of the NLF-FSW wing at all 144 mean phases (hence, between $\bar{\varphi}_1 = 1.25^\circ$ and $\bar{\varphi}_{144} = 358.75^\circ$ in steps of $\Delta\varphi = 2.5^\circ$) as function of the pitch oscillation amplitude. Test conditions: $Re_c = 10 \times 10^6$, $M = 0.78$, $\bar{\alpha} = 1^\circ$, and $k = 0.30$. (a): $\Delta\alpha_{pp} = 0.2^\circ$; (b): $\Delta\alpha_{pp} = 0.4^\circ$; (c): $\Delta\alpha_{pp} = 0.6^\circ$; (d): $\Delta\alpha_{pp} = 0.8^\circ$; (e): $\Delta\alpha_{pp} = 1.0^\circ$.

be deduced. First of all, the results clearly pinpoint out that absolute motions of the transition location over the suction side of the wing as small as $\mathcal{O}(10^{-4})$ m can accurately be resolved by the time-resolved cryoTSP measurement technique. A second interesting aspect that becomes clear from Fig. 6 is that at the majority of combinations of y/b and $\Delta\alpha_{pp}$ the sinusoidal pitch motion is clearly visible in the trend of the values of $\Delta x_{Tr}/c$ over one time-averaged pitch oscillation period. One clear exception to this general trend appears at $y/b = 0.718$ (i.e. around the midplane of the third TSP field), for which, independently of the pitch oscillation amplitude, barely any changes in the values of $\Delta x_{Tr}/c$ with increasing phase can be observed. At all other shown spanwise locations, an increase in $\Delta\alpha_{pp}$ leads furthermore to a higher maximum absolute shift in the transition location with respect to its mean position. Interestingly, while travelling in spanwise direction from the root to the tip of the wing, a clear decrease in the maximum absolute values of $\Delta x_{Tr}/c$ appears first with a minimum that is reached over the inbound part of the third TSP field, which is followed

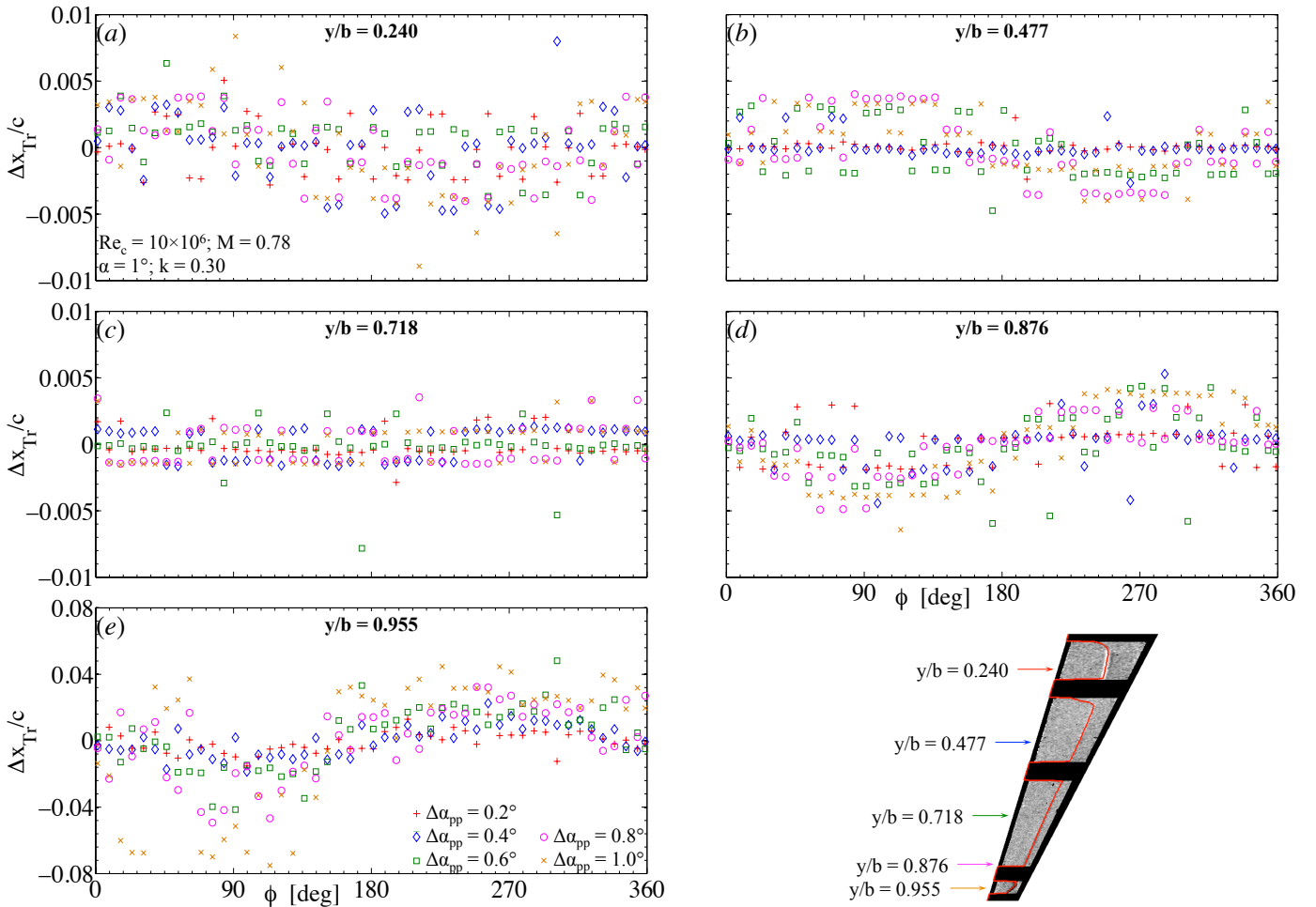


Figure 6. Influence of the oscillation amplitude $\Delta\alpha_{pp}$ on the non-dimensional fluctuation of the laminar-turbulent transition location $\Delta x_{Tr}/c$ in the boundary layer along five spanwise locations y/b on the upper surface of the NLF-FSW wing over one pitch oscillation period. Test conditions: $Re_{\bar{c}} = 10 \times 10^6$, $M = 0.78$, $\bar{\alpha} = 1^\circ$, and $k = 0.30$. (a): $y/b = 0.240$; (b): $y/b = 0.477$; (c): $y/b = 0.718$; (d): $y/b = 0.876$; (e): $y/b = 0.966$.

by a gradual, but distinct recovery towards the tip of the wing at which point the highest peak-to-peak values for $\Delta x_{Tr}/c$ are reached. The results in Fig. 5 and Fig. 6 both show that this behaviour occurs at each of the tested values of $\Delta\alpha_{pp}$ and is more pronounced for higher pitch oscillation amplitudes.

4.2. Variation in mean pitch angle

The influence of a variation in mean pitching angle around which the model performs its forced harmonic pitch motion on the spanwise distribution of the laminar-turbulent transition location is illustrated in Fig. 7 for three pitch oscillation amplitudes at $\bar{\alpha} = 0^\circ$ and $\bar{\alpha} = 1^\circ$. For all shown combinations of $\bar{\alpha}$ and $\Delta\alpha_{pp}$, the Reynolds number and Mach number of the incoming free-stream, as well as the reduced pitch frequency remained constant at $Re_{\bar{c}} = 10 \times 10^6$, $M = 0.78$, and $k = 0.3$,

respectively. At each pitch oscillation amplitude, the trends of the curves show that a decrease of

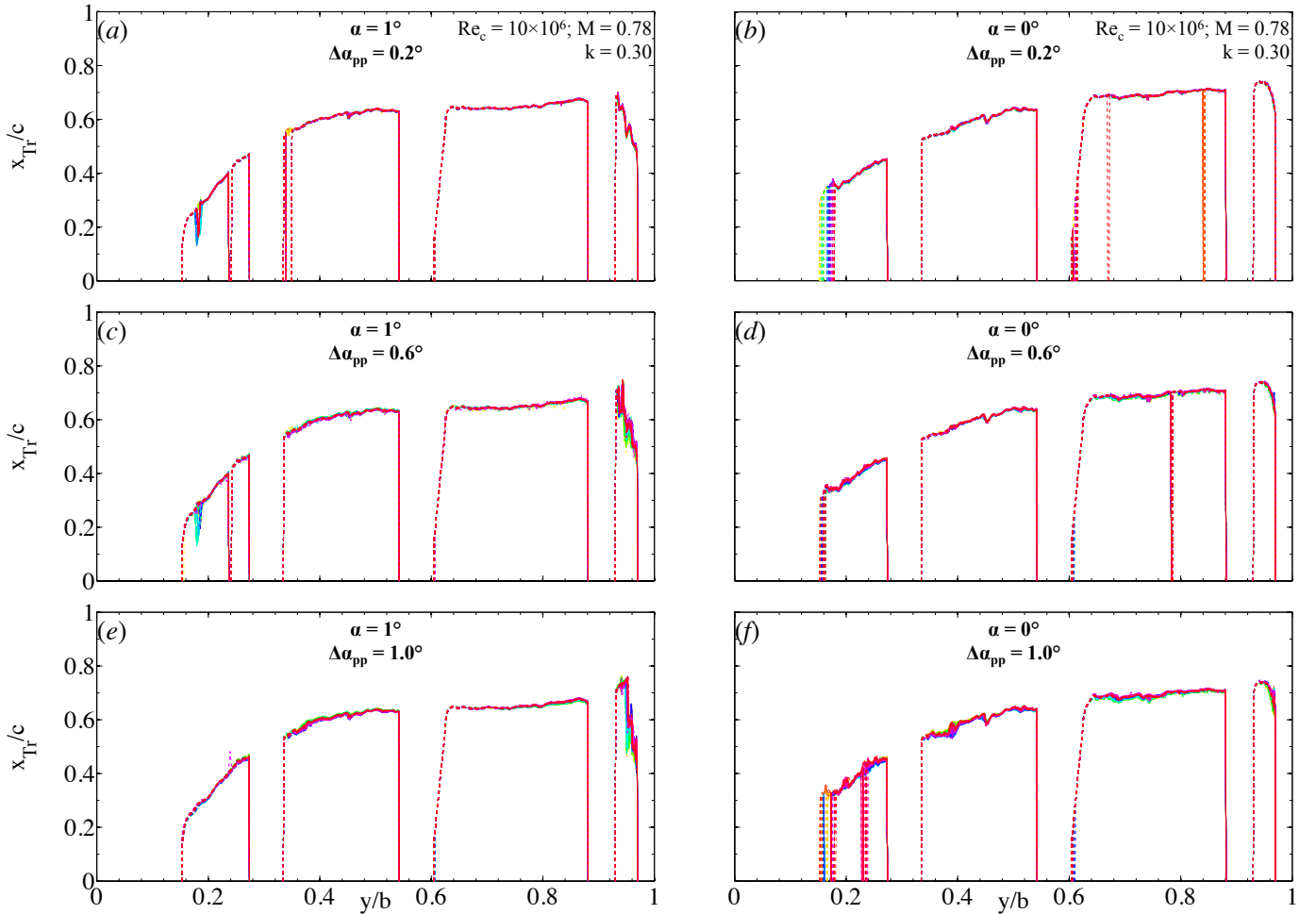


Figure 7. Overlay of spanwise distribution of the non-dimensional transition location x_{Tr}/c in the boundary layer over the upper surface of the NLF-FSW wing at all 144 mean phases (hence, between $\bar{\varphi}_1 = 1.25^\circ$ and $\bar{\varphi}_{144} = 358.75^\circ$ in steps of $\Delta\varphi = 2.5^\circ$) for three different pitch oscillation amplitudes at $\bar{\alpha} = 1^\circ$ (left column) and $\bar{\alpha} = 0^\circ$ (right column).

Test conditions: $Re_{\bar{c}} = 10 \times 10^6$, $M = 0.78$, and $k = 0.30$. (a): $\bar{\alpha} = 1^\circ$, $\bar{\alpha} = 0^\circ$, $\Delta\alpha_{pp} = 0.2^\circ$; (b): $\Delta\alpha_{pp} = 0.2^\circ$; (c): $\bar{\alpha} = 1^\circ$, $\Delta\alpha_{pp} = 0.6^\circ$; (d): $\bar{\alpha} = 0^\circ$, $\Delta\alpha_{pp} = 0.6^\circ$; (e): $\bar{\alpha} = 1^\circ$, $\Delta\alpha_{pp} = 1.0^\circ$; (f): $\bar{\alpha} = 0^\circ$, $\Delta\alpha_{pp} = 1.0^\circ$.

the mean pitch angle from $\bar{\alpha} = 1^\circ$ (left column of Fig. 7) to $\bar{\alpha} = 0^\circ$ (right column) induces a downstream shift of the transition location at most spanwise locations, in agreement with the results of the performance test of this forward-swept wing model at $M = 0.78$ and $Re_{\bar{c}} = 16 \times 10^6$ that have been presented in Van Hinsberg et al. (2024). Only over the second TSP field, i.e. for $0.336 \leq y/d \leq 0.542$, the transition moves slightly upstream with decreasing mean pitch angle. The higher stability of the surface boundary layer for lower mean pitch angles results in a somewhat weaker curvature of the transition line along the span of the wing, which becomes particularly visible when focusing on the transition line over the most outbound TSP field. While at $\bar{\alpha} = 1^\circ$ a distinct decrease of the laminar portion of the boundary layer over this section of the suction side of the wing takes place towards the tip of the wing, a much flatter transition distribution (hence, a more constant laminar

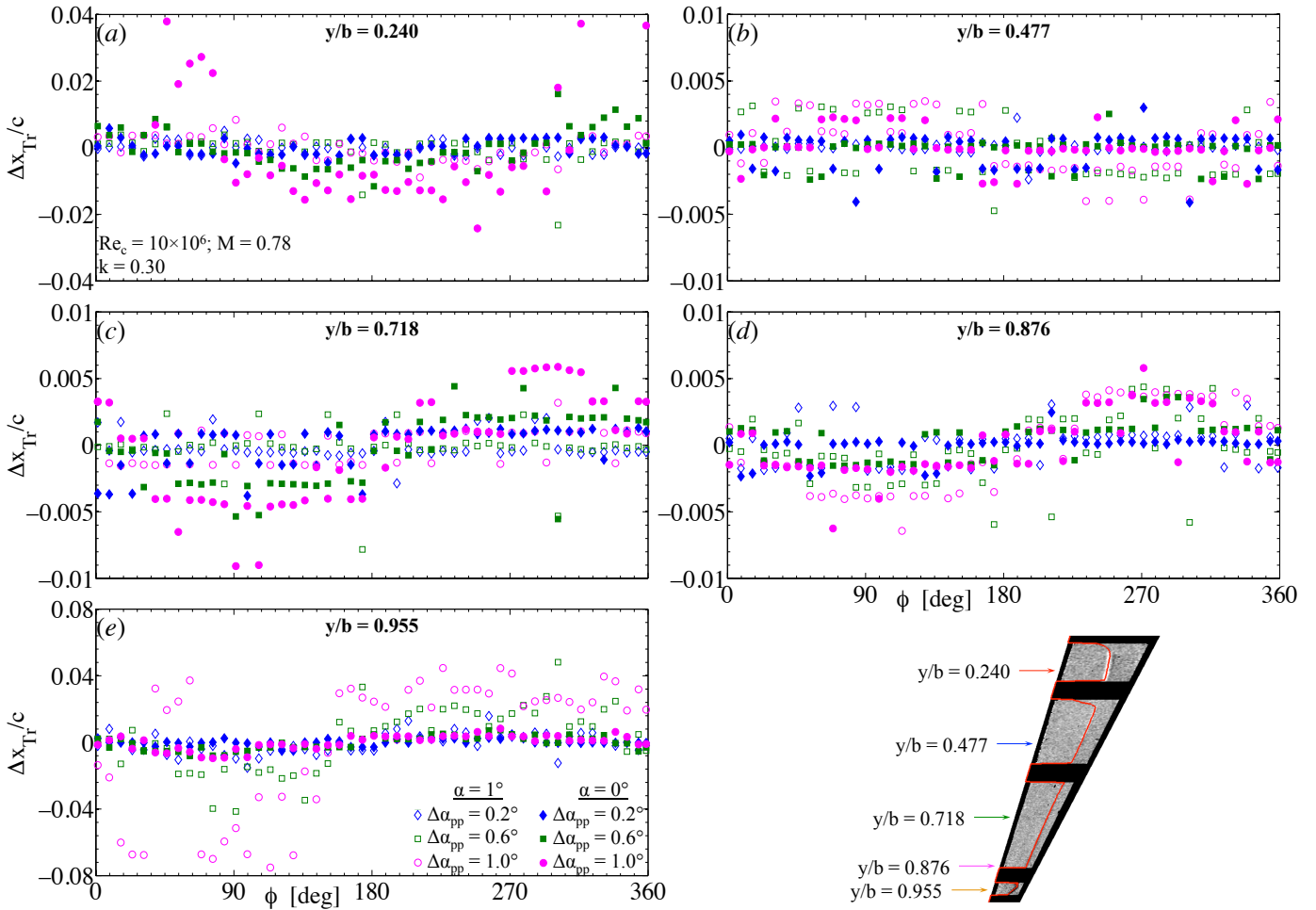


Figure 8. Influence of the oscillation amplitude $\Delta\alpha_{pp}$ and mean incidence angle $\bar{\alpha}$ on the non-dimensional fluctuation of the laminar-turbulent transition location $\Delta x_{Tr}/c$ in the boundary layer along five spanwise locations y/b on the upper surface of the NLF-FSW wing over one pitch oscillation period. Test conditions: $Re_c = 10 \times 10^6$, $M = 0.78$, and $k = 0.30$. (a): $y/b = 0.240$; (b): $y/b = 0.477$; (c): $y/b = 0.718$; (d): $y/b = 0.876$; (e): $y/b = 0.955$.

portion of the boundary layer) is obtained for $\bar{\alpha} = 0^\circ$.

In Fig. 8 the focus is put on the effect of a change in $\bar{\alpha}$ on the dynamics of the spanwise distribution of the transition location over one time-averaged forced pitch oscillation period. To assure once again a clear and concise display of the data, only the results of every third mean phase bin are shown. Unfortunately, no clear overall trend in the behaviour of $\Delta x_{Tr}/c$ as function of $\bar{\varphi}$ can be recognised for the various combinations of $\bar{\alpha}$ and $\Delta\alpha_{pp}$. Depending on the spanwise location y/b , different trends can be observed instead. Over the most inbound (i.e. the first) and the third TSP field, the decrease in mean pitch angle leads to an increase of in particular the maximum absolute values of $\Delta x_{Tr}/c$, which results in the appearance of a clearer sinusoidal behaviour of $\Delta x_{Tr}/c$ over the time-averaged pitch oscillation period (Fig. 8a and 8c). This counts most of all for the highest tested pitch oscillation of $\Delta\alpha_{pp} = 1.0^\circ$. While only a minor effect of $\bar{\alpha}$ is found on the dynamics of

the transition location over the second TSP field (e.g. at $y/b = 0.477$ in Fig. 8b), a distinct decrease in the values of $\Delta x_{Tr}/c$ has been obtained for spanwise locations close to the tip of the wing, as shown in Fig. 8d and 8e for $y/b = 0.876$ and 0.955 . At both spanwise locations, a strong flattening of the $\Delta x_{Tr}/c(\bar{\varphi})$ curves has taken place at all three oscillation amplitudes for $\bar{\alpha} = 0^\circ$ with respect to the corresponding curves for $\bar{\alpha} = 1^\circ$. Hence, at the former mean pitch angle the location of the laminar-to-turbulent transition in the boundary layer in the vicinity of the wing tip thus shows a severe increase in independence on the phase angle during a forced pitch oscillation.

4.3. Variation in reduced pitch frequency

The tested variation in reduced pitch frequency spanned the range of $k = 0-1.0$, which equals a dimensional pitch frequency f_{pitch} between 0 Hz and 74–92 Hz, the exact value of the latter being dependent on the combination of Mach and Reynolds number. The exemplary results in Fig. 9 ($Re_{\bar{c}} = 10 \times 10^6$, $M = 0.78$, $\bar{\alpha} = 1^\circ$, and $\Delta\alpha_{pp} = 0.2^\circ$) demonstrate that an increase in k has its main influence on the dynamics of the transition location over one time-averaged pitch oscillation period close to the tip of the wing. A similar conclusion can be drawn from the graphs for $\Delta x_{Tr}/c$

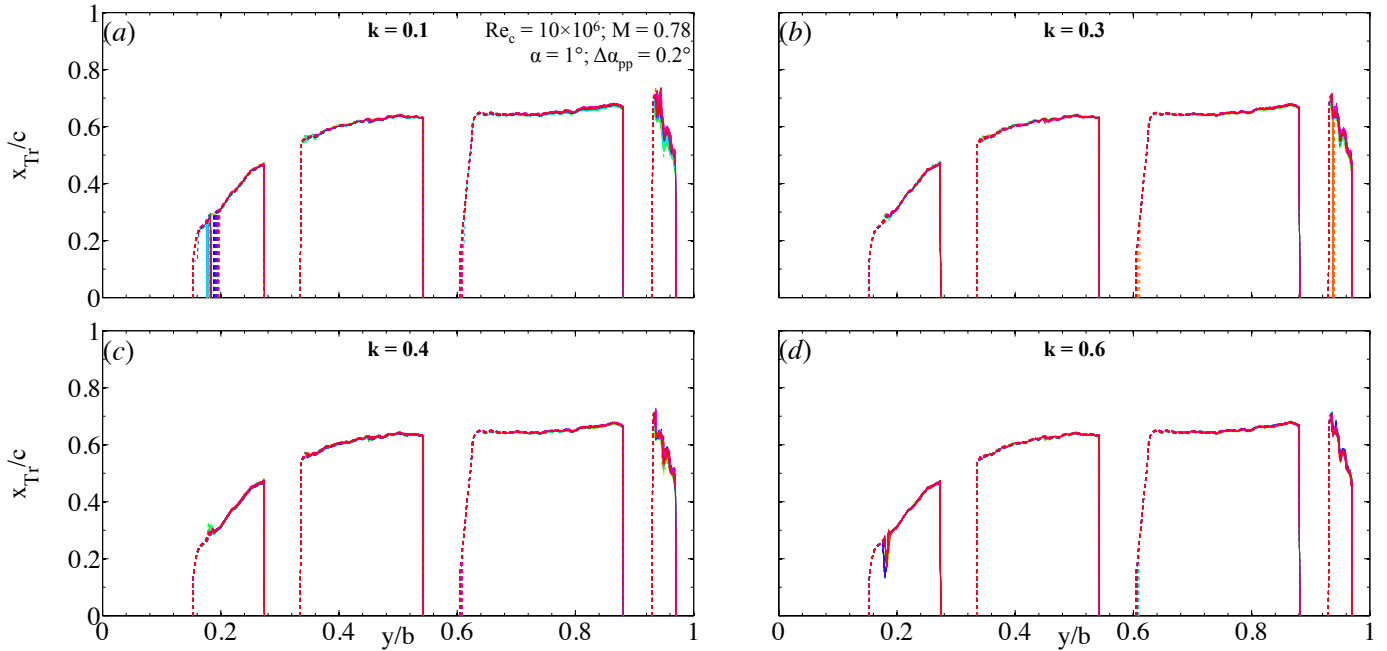


Figure 9. Overlay of spanwise distribution of the non-dimensional transition location x_{Tr}/c in the boundary layer over the upper surface of the NLF-FSW wing at all 144 mean phases (hence, between $\bar{\varphi}_1 = 1.25^\circ$ and $\bar{\varphi}_{144} = 358.75^\circ$ in steps of $\Delta\varphi = 2.5^\circ$) as function of the reduced oscillation frequency k . Test conditions: $Re_{\bar{c}} = 10 \times 10^6$, $M = 0.78$, $\bar{\alpha} = 1^\circ$, and $\Delta\alpha_{pp} = 0.2^\circ$. (a): $k = 0.1$; (b): $k = 0.3$; (c): $k = 0.4$; (d): $k = 0.6$.

as function of $\bar{\varphi}$ in Fig. 10, in which only the results of every third mean phase bin are presented to recognise the trends. Over the inbound half span of the wing (e.g. $y/b = 0.240$ and 0.477) the

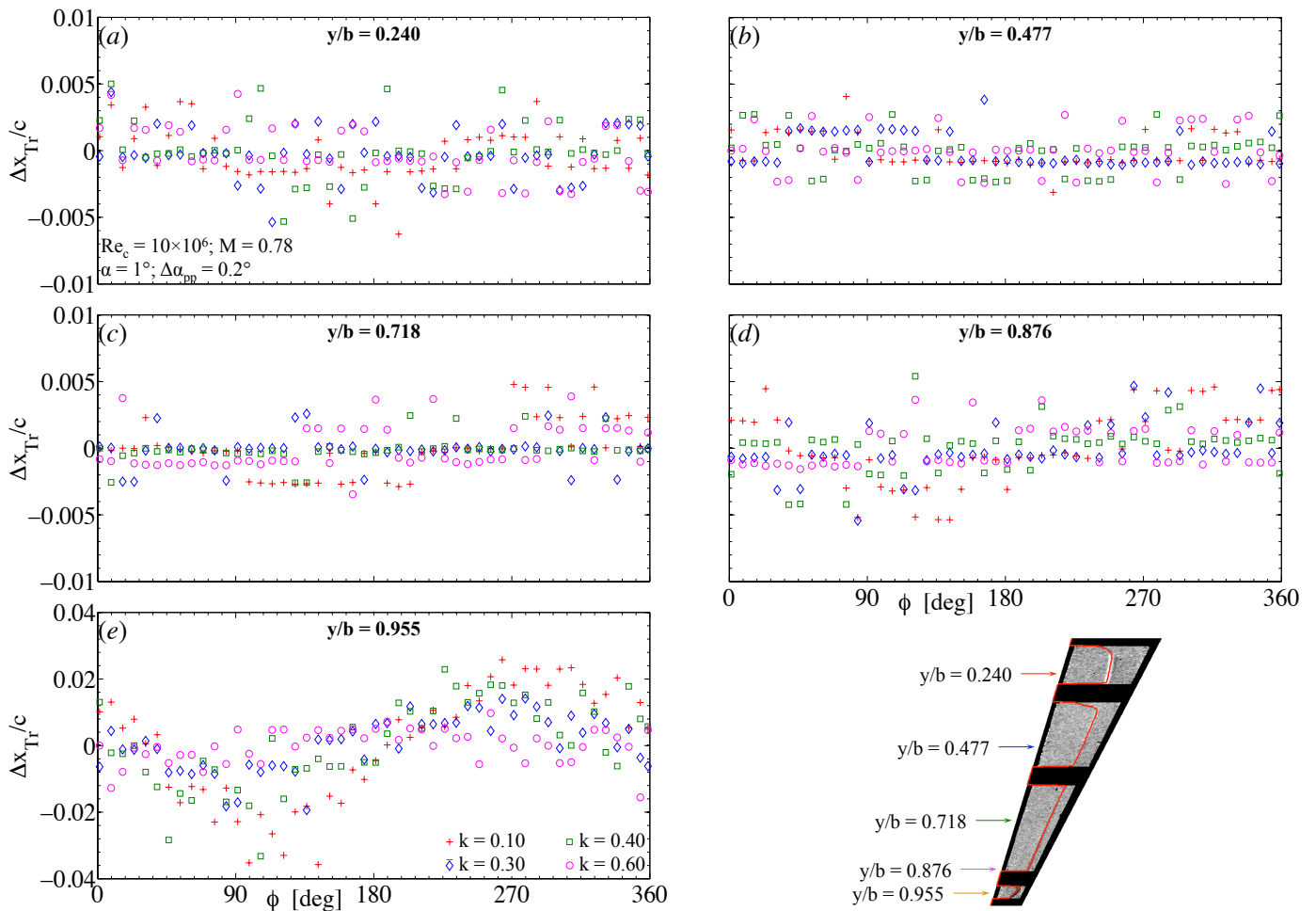


Figure 10. Influence of the reduced pitch frequency k on the non-dimensional fluctuation of the laminar-turbulent transition location $\Delta x_{Tr}/c$ in the boundary layer along five spanwise locations y/b on the upper surface of the NLF-FSW wing over one pitch oscillation period. Test conditions: $Re_{\bar{c}} = 10 \times 10^6$, $M = 0.78$, $\bar{\alpha} = 1^\circ$, and $\Delta\alpha_{pp} = 0.2^\circ$. (a): $y/b = 0.240$; (b): $y/b = 0.477$; (c): $y/b = 0.718$; (d): $y/b = 0.876$; (e): $y/b = 0.966$.

transition location is found to be relatively unaffected by a variation in k . In contrast, we not only observe a clear decrease in $\Delta x_{Tr}/c$ for a larger reduced pitch frequency at $y/b = 0.718$, 0.876 , and 0.966 , hence, over the outbound half span of the wing. But at the same time, by comparing the graphs at these spanwise locations we also note a stronger reduction in $\Delta x_{Tr}/c$ with increased k the closer we get to the tip of the wing. The latter two findings are most probably caused by a combination of a weaker bending and torsion of the wing, in particular regarding its outer part, that induces a lower dynamics of the aerodynamic phenomena occurring on the suction surface of the wing while it performs a forced harmonic pitch oscillation.

4.4. Variation in Mach and Reynolds number

The majority of the dynamic model tests were conducted at two different Mach numbers, i.e. $M = 0.73$ and 0.78 , while the variation in Reynolds number was limited for all tests to $Re_{\bar{c}} = 10 \times 10^6$ and 16×10^6 .

Fig. 11 and 12 present the effect of a change in the value of the first of both studied flow parameters, while keeping both the Reynolds number ($Re_{\bar{c}} = 10 \times 10^6$) and the model pitch parameters ($\bar{\alpha} = 1^\circ$, $\Delta\alpha_{pp} = 0.2^\circ$, and $k = 0.30$) constant. Based on the analysis of the time-resolved TSP data

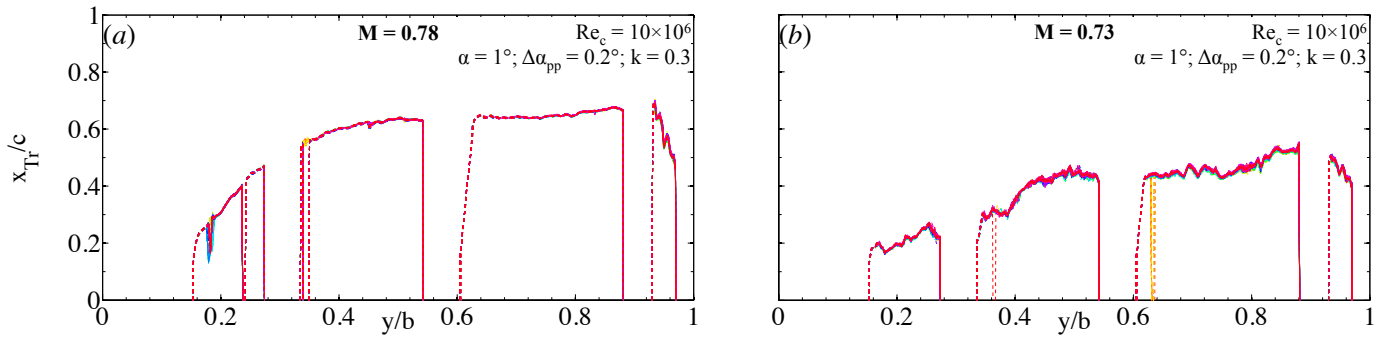


Figure 11. Overlay of spanwise distribution of the non-dimensional transition location x_{Tr}/c in the boundary layer over the upper surface of the NLF-FSW wing at all 144 mean phases (hence, between $\bar{\varphi}_1 = 1.25^\circ$ and $\bar{\varphi}_{144} = 358.75^\circ$ in steps of $\Delta\varphi = 2.5^\circ$) as function of the Mach number. Test conditions: $Re_{\bar{c}} = 10 \times 10^6$, $\bar{\alpha} = 1^\circ$, $\Delta\alpha_{pp} = 0.2^\circ$, and $k = 0.30$. (a): $M = 0.78$; (b): $M = 0.73$.

we obtained during the past performance test of this NLF forward-swept wing at different Mach numbers within the range $M = 0.76$ – 0.80 in ETW, we could derive that an increase in Mach number induces a clear downstream motion of the global transition location over most of the span of the wing (Van Hinsberg et al., 2024). This behaviour matches well with the currently obtained spanwise distributions of the transition for $M = 0.78$ (Fig. 11a) and $M = 0.73$ (Fig. 11b), showing that a favourable laminarisation of the flow over the suction side of the wing is achieved at higher flight-relevant Mach numbers. The distinct fluctuations of the transition along the spanwise section for every value of $\bar{\varphi}$ at $M = 0.73$ in Fig. 11b indicate the presence of a cross-flow-initiated transition on this wing. However, the much smoother transition lines at $M = 0.78$ suggest that the boundary layer transition mechanism has most probably changed from cross-flow-initiated to shock-induced while passing from the former to the latter Mach number.

This switch in boundary layer transition mechanism has also a clear effect on the dynamics of the transition location over the time-averaged pitch oscillation. Both in Fig. 11 and 12 a distinct decrease in the transition fluctuations $\Delta x_{Tr}/c$ over one oscillation period is noticed in particular over the second (e.g. for $y/b = 0.477$) and third (e.g. for $y/b = 0.718$ and 0.876) TSP fields. This also results in the disappearance of the sinusoidal behaviour of the $\Delta x_{Tr}/c(\bar{\varphi})$ curve at these spanwise locations. Surprisingly, the values of $\Delta x_{Tr}/c$ over the most inbound and most outbound TSP fields

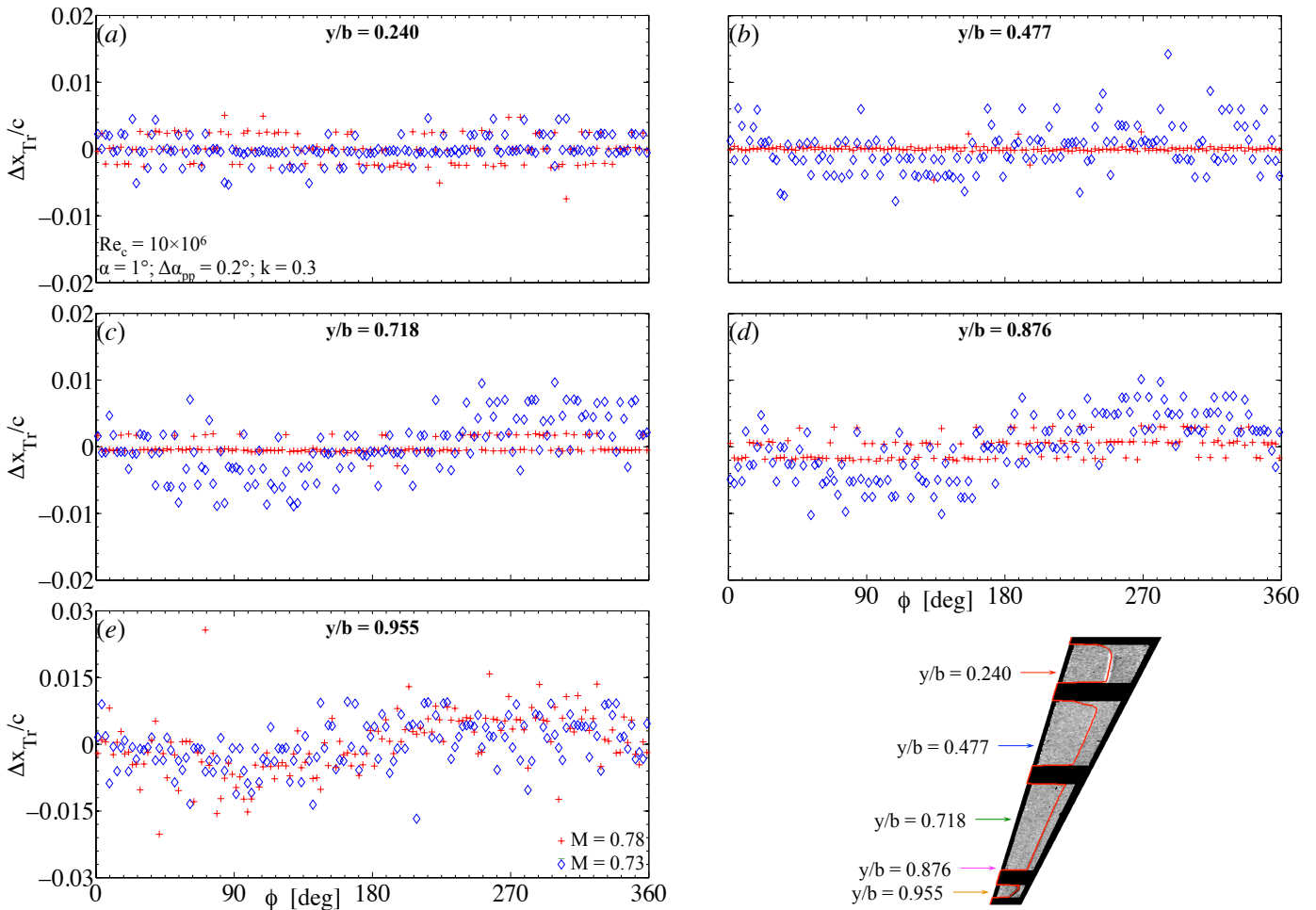


Figure 12. Influence of the Mach number M on the non-dimensional fluctuation of the laminar-turbulent transition location $\Delta x_{Tr}/c$ in the boundary layer along five spanwise locations y/b on the upper surface of the NLF-FSW wing over one pitch oscillation period. Test conditions: $Re_{\bar{c}} = 10 \times 10^6$, $\bar{\alpha} = 1^\circ$, $\Delta\alpha_{pp} = 0.2^\circ$, and $k = 0.3$. (a): $y/b = 0.240$; (b): $y/b = 0.477$; (c): $y/b = 0.718$; (d): $y/b = 0.876$; (e): $y/b = 0.966$.

(Fig. 12a and 12e) hardly seem to be affected by a change in Mach number.

The influence of the flight-relevant Reynolds number on the dynamics of the spanwise transition location during forced harmonic pitch oscillations is shown in Fig. 13 and 14. The Mach number is in this case fixed at $M = 0.73$, while the model pitch parameters ($\bar{\alpha}$, $\Delta\alpha_{pp}$, and k) are equal to those in the previous Fig. 11 and 12. While at $Re_{\bar{c}} = 10 \times 10^6$ an almost perfectly continuous transition line is detected along the span of the wing at each value of $\bar{\varphi}$, an increasing amount of turbulent wedges appears over the TSP fields 1 to 3 in the test cases at the higher Reynolds number. These wedges are most probably caused by surface imperfections or settled particles near the leading edge that trigger the transition to turbulence, and become increasingly more apparent at higher Reynolds numbers. Although the presence of these wedges hinders a precise detection and comparison of the transition locations at the spanwise locations at which they appear, it can

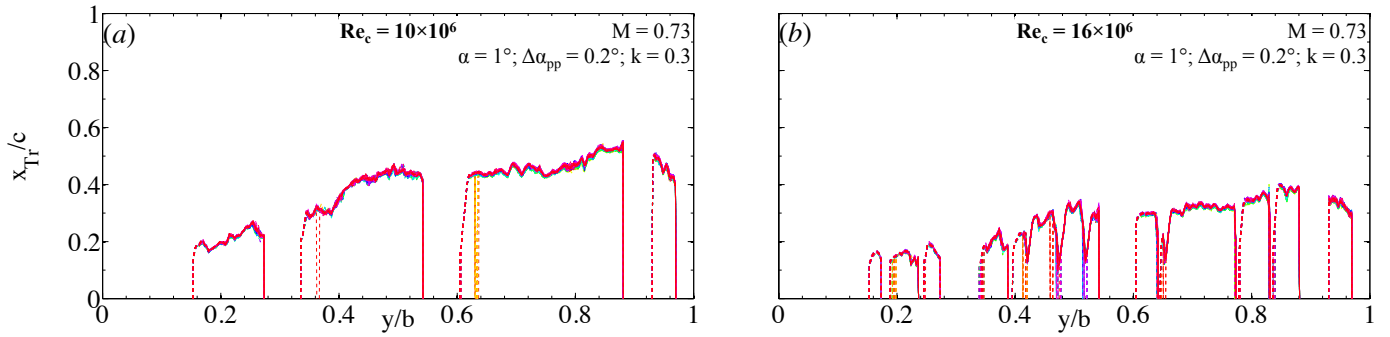


Figure 13. Overlay of spanwise distribution of the non-dimensional transition location x_{Tr}/c in the boundary layer over the upper surface of the NLF-FSW wing at all 144 mean phases (hence, between $\bar{\varphi}_1 = 1.25^\circ$ and $\bar{\varphi}_{144} = 358.75^\circ$ in steps of $\Delta\varphi = 2.5^\circ$) as function of the Reynolds number. Test conditions: $M = 0.73$, $\bar{\alpha} = 1^\circ$, $\Delta\alpha_{pp} = 0.2^\circ$, and $k = 0.30$.
 (a): $Re_{\bar{c}} = 10 \times 10^6$; (b): $Re_{\bar{c}} = 16 \times 10^6$.

be deduced from the transition curves at all other spanwise positions that also at the combination $Re_{\bar{c}} = 16 \times 10^6$ and $M = 0.73$ the main transition mechanism over the wing is cross-flow-initiated. This is contrary to the observations made in the past performance test, for which at the higher of the current two tested Reynolds numbers a clear shock-initiated transition was present over most of the wing. It has to be mentioned though, that in the latter case the Mach number was slightly higher, i.e. $M = 0.76$ instead of $M = 0.73$. Moreover, the current results show an upstream shift of the global transition line over the span of the wing at each mean phase angle with increasing Reynolds number. Also this behaviour was not found in the performance test at $M = 0.78$, most likely because at higher Mach numbers compressibility effects lead to an increased stability of the boundary layer.

Interestingly, the curves in Fig. 14 indicate only a minor effect of the Reynolds number on the dynamic behaviour of the global transition location. This counts both for the presence or absence of the sinusoidal trend of the curves and for the actual values of $\Delta x_{Tr}/c$.

5. Conclusions

The temporal and spatial behaviour of the laminar-turbulent boundary-layer transition location across the suction surface of a newly-designed NLF-forward-swept wing, in combination with a fuselage-belly-fairing, for future commercial transport aircraft was measured optically in ETW by making use of the measurement technique Temperature-Sensitive Paint. The tests were performed at flight-relevant steady flow conditions, while a pitch oscillator, specially designed within this project for dynamic model testing in ETW, was used to set the wing model into a forced harmonic pitch oscillation. In this way, the effect of variations not only in the Mach and Reynolds number, but also in the mean angle, the amplitude, and the reduced frequency of the forced harmonic

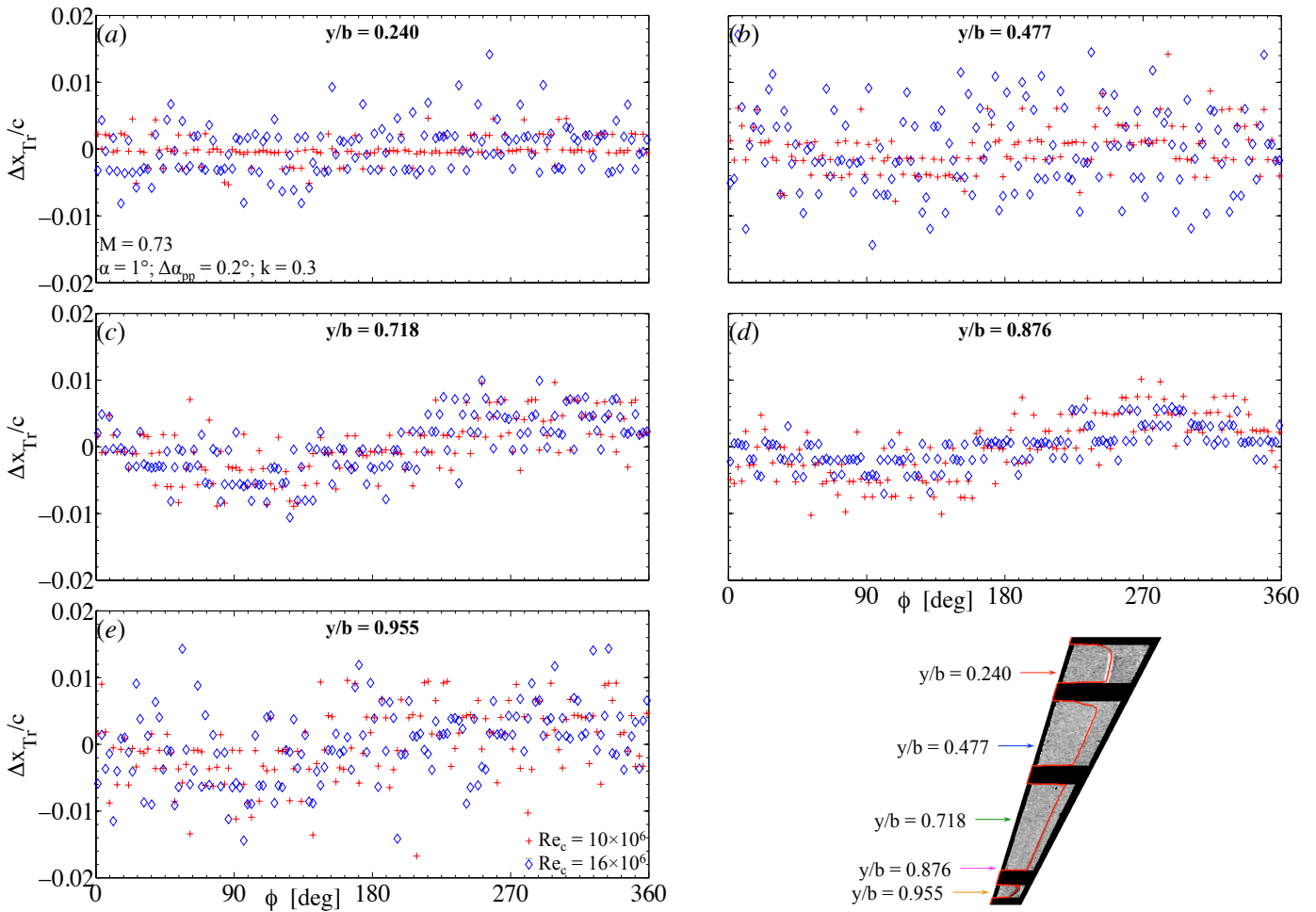


Figure 14. Influence of the Reynolds number number $Re_{\bar{c}}$ on the non-dimensional fluctuation of the laminar-turbulent transition location $\Delta x_{Tr}/c$ in the boundary layer along five spanwise locations y/b on the upper surface of the NLF-FSW wing over one pitch oscillation period. Test conditions: $M = 0.73$, $\bar{\alpha} = 1^\circ$, $\Delta\alpha_{pp} = 0.2^\circ$, and $k = 0.3$. (a): $y/b = 0.240$; (b): $y/b = 0.477$; (c): $y/b = 0.718$; (d): $y/b = 0.876$; (e): $y/b = 0.966$.

pitch oscillations on the highly dynamic motion-induced aerodynamics of the forward-swept wing could be investigated experimentally.

The analysis of the influence of the isolated and combined changes in the flight relevant Mach ($M = 0.73 \rightarrow 0.78$) and Reynolds ($Re_{\bar{c}} = 10 \times 10^6 \rightarrow 16 \times 10^6$) numbers on the spanwise transition distribution showed an opposite behaviour. For both tested Reynolds numbers at constant Mach number and mean pitch angle ($M = 0.73$ and $\bar{\alpha} = 1^\circ$), a cross-flow-initiated transition was present over most parts of the wing. A Reynolds-number effect was clearly visible in form of an upstream motion of the global transition line at the higher of the two Reynolds numbers. In turn, an increase in the Mach number (at $Re_{\bar{c}} = 10 \times 10^6$ and $\bar{\alpha} = 1^\circ$) caused a shift of the transition region in downstream direction for longer laminar running lengths over the complete span of the wing. Moreover, while passing from the lower to the higher Mach number, the boundary layer transition

mechanism changed from cross-flow-initiated to shock-induced.

With the exception of the Reynolds number, a strong dependency of both the trend and the values of the fluctuations of the detected spanwise transition pattern and chordwise location over one time-averaged pitch oscillation period on the studied flow and model parameters was found. An increase in the pitch oscillation amplitude, while keeping both the mean pitch angle and reduced pitch frequency constant, resulted for example in a higher maximum absolute shift in the transition location around the mean pitch angle over one oscillation period. The actual amount of increase of those fluctuations depended on the spanwise position, though: while close to the root and tip of the wing the largest growth in fluctuations with increasing pitch oscillation amplitude occurred, a local minimum was found over the inbound part of the third TSP field. An increase in reduced pitch frequency, on the other hand, induced over the outbound half span of the wing a distinct decrease in the amount of shifting of the transition location in chord direction. This reduction with increased reduced frequency got higher the more the tip of the wing was approached, most probably being caused by the prevention of a significant bending and torsion of the wing with faster pitch motion. In contrast, over the inbound half span of the wing, the transition location was found to be relatively unaffected by the reduced pitch frequency. The comparison between the amount of motion of the spanwise transition line over one pitch oscillation at both Mach numbers revealed that the most significant changes in the dynamics of the transition pattern due to a change in Mach number occurred over the center part of the wing, where both a distinct decrease and the disappearance of the sinusoidal behaviour of the transition fluctuations were found. By contrast, the transition pattern over the inner and outer parts of the wing seemed to be largely independent on a change in Mach number.

Acknowledgements

Support from Carsten Fuchs at DLR Systemhaus Technik is gratefully acknowledged for the model preparation with respect to the TSP measurements, in particular for the surface treatment of the TSP layer. The authors would also like to thank Tobias Kleindienst and Tobias Herrmann of the DLR Institute of Aerodynamics and Flow Technology for the copper-tape and wiring installation in the TSP pockets and for test preparations, respectively. Additionally, we would like to thank the wind tunnel team at ETW for their active support during the test.

Funding

The model design and manufacturing, the wind tunnel experiments, and data analysis were conducted within the framework of the ECOWING and ULTIMATE projects, which provided organ-

isational support for this research. The funding of this work by the Federal Ministry for Economic Affairs and Climate Action (BMWK) for ECOWING (KoPa 33 grant) and ULTIMATE (LuFo 20A2101C) is also gratefully acknowledged.

Nomenclature

$\bar{\alpha}$	Mean / static pitch angle [°]
$\Delta\alpha_{pp}$	Peak-to-peak pitch oscillation amplitude [°]
$\Delta\alpha_{sweep}$	Sweep angular velocity [° s ⁻¹]
$\Delta\varphi$	Phase bin width of pitch oscillation period [°]
Δx_{Tr}	Fluctuation in pitch oscillation amplitude [m]
λ	Wavelength [m]
φ_{LE}	Wing leading edge sweep angle [°]
φ_{TE}	Wing trailing edge sweep angle [°]
$\bar{\varphi}$	Mean phase of pitch oscillation period [°]
b	Wing half span [m]
c_{root}	Root chord length [m]
c_{tip}	Tip chord length [m]
\bar{c}	Mean chord length [m]
E_{nr}	Activation energy for the non-radiative process [J kg ⁻¹]
f_{cam}	Camera recording frequency [s ⁻¹]
f_{pitch}	Pitch frequency [s ⁻¹]
I	Luminescent intensity [cd]
I_{ref}	Reference luminescent intensity [cd]
k	Reduced pitch frequency [-]
M	Mach number [-]
P	Power [J s ⁻¹]
P_{max}	Maximum power [J s ⁻¹]
p_0	Total pressure [kg m ⁻¹ s ⁻²]
R	Universal gas constant [J kg ⁻¹ K ⁻¹]
Re_x	Reynolds number based on reference length x [-]
T	Temperature [K]
t_{exp}	Camera exposure time [s]
U_∞	Free-stream velocity [m s ⁻¹]
x	Position along the chord of the wing [m]
x_{Tr}	Boundary layer transition location along the chord of the wing [m]
y	Position along the span of the wing [m]

References

- Costantini, M., Henne, U., Risius, S., & Klein, C. (2021, June). A robust method for reliable transition detection in temperature-sensitive paint data. *Aerospace Science and Technology*, 113, 106702. doi: 10.1016/j.ast.2021.106702
- Crouch, J. (2015). Boundary-layer transition prediction for laminar flow control (Invited). In *45th AIAA Fluid Dynamics Conference, Dallas, TX, USA*. doi: 10.2514/6.2015-2472
- Egami, Y., Fey, U., Klein, C., Quest, J., Ondrus, V., & Beifuss, U. (2012, October). Development of new two-component temperature-sensitive paint (TSP) for cryogenic testing. *Measurement Science and Technology*, 23(11), 115301-1–11. doi: 10.1088/0957-0233/23/11/115301
- Fujino, M., Yoshizaki, Y., & Kawamura, Y. (2003, July–August). Natural-laminar-flow airfoil development for a lightweight business jet. *Journal of Aircraft*, 40(4), 609–615. doi: 10.2514/2.3145
- Giesecke, D., Lehmler, M., Friedrichs, J., Blinstrub, J., Bertsch, L., & Heinze, W. (2018). Evaluation of ultra-high bypass ratio engines for an over-wing aircraft configuration. *Journal of the Global Power and Propulsion Society*, 2, 493–515. doi: 10.22261/JGPPS.8SHP7K
- Goodman, K., Lipford, W., & Watkins, A. (2016, December). Boundary-layer detection at cryogenic conditions using temperature sensitive paint coupled with a carbon nanotube heating layer. *Sensors*, 16(12), 1–17. doi: 10.3390/s16122062
- Hensch, A.-K., Guntermann, P., Dues, M., Steinbock, J., Siswanto, A., Stockhausen, G., ... Beversdorff, M. (2023). Development of a laser optical point sensor based on the filtered rayleigh scattering technique for use under cryogenic conditions (in german). In *30th Fachtagung Laser-methoden in der Strömungsmesstechnik, München", Germany*.
- Iijima, S. (1991, November). Helical microtubules of graphitic carbon. *Nature*, 354(6348), 56–58. doi: 10.1038/354056a0
- International Air Transport Association (IATA). (2023). *Net zero 2050: sustainable aviation fuels*. Retrieved from <https://www.iata.org/en/iata-repository/pressroom/fact-sheets/fact-sheet---alternative-fuels/> (Accessed 24 April 2024)
- Joslin, R. (1998, January). Aircraft laminar flow control. *Annual Review of Fluid Mechanics*, 30, 1–29. doi: 10.1146/annurev.fluid.30.1.1
- Klein, C., Henne, U., Sachs, W., Beifuss, U., Ondrus, V., Bruse, M., ... Löhr, M. (2014). Application of Carbon Nanotubes (CNT) and Temperature-Sensitive Paint (TSP) for the detection of boundary layer transition. In *52nd AIAA Aerospace Science Meeting, National Harbor, MD, USA*. doi: 10.2514/6.2014-1482

- Klein, C., Henne, U., Yorita, D., Beifuss, U., Ondrus, V., Hensch, A.-K., ... Quest, J. (2017). Application of Carbon Nanotubes and Temperature-Sensitive Paint for the detection of boundary layer transition under cryogenic conditions. In *55th AIAA Aerospace Science Meeting, Grapevine, TX, USA*.
- Krishnan, K., Bertram, O., & Seibel, O. (2017, August). Review of hybrid laminar flow control systems. *Progress in Aerospace sciences*, 93, 24–52. doi: 10.1016/j.paerosci.2017.05.005
- Lange-Schmuckall, F. (2022). *Aerodynamics of forward and backward swept wings with an over-wing-nacelle*. Ph.D. Thesis, Technische Universität Braunschweig, Germany. doi: 10.57676/qde0-ak32
- Liu, T., Salazar, D., & Crafton, J. (2021, October). Extraction of skin friction topology of turbulent wedges on a swept wing in transonic flow from surface temperature images. *Experiments in Fluids*, 62(215), 1–24. doi: 10.1007/s00348-021-03305-5
- Liu, T., Sullivan, J., Asai, K., Klein, C., & Egami, Y. (2021). *Pressure and Temperature Sensitive Paints (2nd edition)*. Springer. doi: 10.1007/978-3-030-68056-5
- Redeker, G., Horstmann, K., Quast, A., Dressler, U., & Bieler, H. (1990). Flight tests with a natural laminar flow glove on a transport aircraft. In *AIAA Flight Simulation Technologies Conference and Exhibit, Dayton, OH USA*. doi: 10.2514/6.1990-3044
- Saeed, T., Graham, W., Babinsky, H., & Hall, C. (2010). Boundary-layer suction system design for application to a laminar flying wing aircraft. In *28th AIAA Applied Aerodynamics Conference, Chicago, IL, USA*. doi: 10.2514/6.2010-4379
- Schlichting, H., & Gersten, K. (2016). *Boundary layer theory (9th Edition)*. Springer. doi: 10.1007/978-3-662-52919-5
- Seitz, A., Kruse, M., Wunderlich, T., Bold, J., & Heinrich, L. (2011). The DLR project LamAIR: design of a nlr forward swept wing for short and medium range transport application. In *29th AIAA Applied Aerodynamics Conference, Honolulu, HI, USA*. doi: 10.2514/6.2011-3526
- Semmelmann, J., Quix, H., & Quest, J. (2013). Enhancement of the Stereo Pattern Tracking technique for model deformation assessment at ETW. In *51st AIAA Aerospace Science Meeting, Grapevine, TX, USA*.
- Streit, T., Wedler, S., & Kruse, M. (2015, November). DLR natural and hybrid transonic laminar wing design incorporating new methodologies. *The Aeronautical Journal*, 119(1221), 1303–1326. doi: 10.1017/S0001924000011283
- Thiessen, R., & Schüle, E. (2019, September). Infrared thermography and DIT of quadcopter rotor blades using laser heating. *Proceedings*, 27(1: 31), 1–5. doi: 10.3390/proceedings2019027031

- Van Hinsberg, N., Henne, U., Weiss, A., Risius, S., Klein, C., Ondrus, V., ... Guntermann, P. (2024). Temperature-Sensitive Paint measurements in the European Transonic Windtunnel for investigation of the natural laminar flow on an innovative forward-swept wing. *Submitted to CEAS Aeronautical Journal*.
- Weiss, A., Wolf, C., Kaufmann, K., Braukmann, J., Heineck, J., & Raffel, M. (2020, February). Unsteady boundary-layer transition measurements and computations on a rotating blade under cyclic pitch conditions. *Experiments in Fluids*, 61(2), 1–16. doi: 10.1007/s00348-020-2899-7
- Wolf, C. (2023). *Differential infrared thermography for rotor aerodynamics*. Gottfried Wilhelm Leibniz Universität, Hannover, Germany. doi: 10.15488/14143
- Yorita, D., Lemarechal, J., Klein, C., Fujita, K., & Nagai, H. (2020). Transition detection methods in a pitch-sweep test by means of TSP using lifetime and intensity measurements. In *58th AIAA Aerospace Science Meeting, Orlando, FL, USA*. doi: 10.2514/6.2020-0296